arXiv:astro-ph/0208338v1 18 Aug 2002

Unveiling the Kinematics and Dynamics of Ionized gas in the Nearby Irregular Galaxy NGC 4449

Margarita Valdez–Gutiérrez[1,2,3], Margarita Rosado[4], Ivânio Puerari[1], Leonid Georgiev[4], Jordanka Borissova[5], and Patricia Ambrocio–Cruz[4]

ABSTRACT

A detailed kinematic analysis of ionized gas in the nearby irregular galaxy NGC 4449 is presented. Observations are conducted in the spectral lines of Hα and [S II]. Our scanning Fabry–Perot interferometric observations are presented from both a global as well as a local perspective. We have analysed the global velocity field, the spatially extended diffuse gaseous component (DIG), the H II region populations, and, furthermore, have determined the rotation curve based on the heliocentric radial velocities of the global Hα spatial distribution.

Our results for NGC 4449 show that the optical velocity field has a decreasing value in radial velocity along the optical bar from NE to SW, presenting an anticorrelation relative to the outer velocity field of the H I component. This is in agreement with previous studies. The DIG component that permeates the entire galaxy was analysed (up to a limiting surface brightness of $\sim 3.165\times10^{-5}$ ergs cm^{-2} s^{-1} steradian^{-1}) in terms of its radial velocity field as well as its velocity dispersions. We find that the diffuse gas component presents peculiar kinematical features such as abrupt velocity gradients and highly supersonic velocity dispersions ($\sigma \sim 4$ times the values of the nearest H II regions) but that its kinematical and dynamical influence is important on both global and local scales. The optical rotation curve of this nearby irregular shows that the NE sector rotates like a solid body ($V_{rot} \sim$40 km s^{-1} at R =2 kpc). In contrast, for the SW side, our results are not conclusive; the behavior of the gas at those locations is chaotic. We conclude that the origin of such complex kinematics and dynamics is undoubtedly related to the aftermath of an interaction experienced by this galaxy in the past.

Subject headings: galaxies: irregular – galaxies: individual (NGC 4449) – galaxies: kinematics and dynamics – galaxies: ISM – ISM: general

1. Introduction

In terms of frequency of occurrence, the most common morphology for galaxies in the Universe are the Irregular (Irr) strain (Gallager & Hunter 1984). Irregulars may serve as morphological Rosetta stones bridging the low and high redshift Universe (Block et al. 2001). Historically, drawings of Irrs may be found as early as 1847 (the Large Magellanic Cloud, classified by Hubble as an irregular, was sketched by Sir John Herschel in that year). When imaged in the near–infrared, a handful of irregulars betray a magnificent – albeit weak – spiral density wave; examples are NGC 5195 and NGC 922 (the latter galaxy even shows

---

[1] Instituto Nacional de Astrofísica, Optica y Electrónica; Calle Luis Enrique Erro 1, 72840, Tonantzintla, Puebla, México; mago@inaoep.mx, puerari@inaoep.mx

[2] Current Address: Observatoire de Paris–LERMA, 61, Avenue de l'Observatoire, 75014, Paris, France; margarita.valdez@obspm.fr

[3] Postdoctoral CONACyT Fellow

[4] Instituto de Astronomía, UNAM; Apartado Postal 70–264, 04510, México, D. F., México; margarit@astroscu.unam.mx, georgiev@astroscu.unam.mx, patricia@astroscu.unam.mx

[5] Institute of Astronomy, Bulgarian Academy of Sciences and Isaac Newton Institute of Chile Bulgarian Branch, Bulgaria; 72 Tsarigradsko chaussèe, BG –1784 Sofia, Bulgaria; jura@haemimont.bg

spiral arm modulation). Generally, however, there is no decoupling of the Population I and Population II disks; many optical irregulars remain irregular in the near–infrared. One of the most intriguing questions yet to be answered is exactly what triggers/drives the formation of stars in galaxies.

Here the Irr species offer unprecedented opportunities, for they are excellent laboratories in which one can examine the star formation process –and its influence on the interstellar medium (ISM)– often in the complete absence of spiral density waves. Furthermore, the existence of fossil interacting features in some of these galaxies makes them worthy of detailed study (Hunter et al. 2000a). The global study of the kinematical behavior of the gas in such environments is dynamically important. The presence of embedded superbubbles, giant H II regions, filaments, supernova remnants (SNRs) and their combined effects, makes the global velocity field of irregular galaxies both stimulating and important to analyze.

The face of the galaxy NGC 4449, a nearby Magellanic type Irr galaxy, is highly peculiar, with Hα streamers and filaments everywhere. Not only does NGC 4449 present giant H II regions, but also a SNR, superbubbles, and a diffuse emission (which embraces almost the entire optical boundary). The faint Hα filament population alluded to above is intriguing; the filaments delineate the inner edge of a 2 kpc diameter H I supershell (Hunter & Gallagher 1997) located at the northwest side of the main optical body. At other wavelengths, there is a body of evidences suggesting a close connection between the diffuse nebulae, the diffuse emission and the X–ray emission from the center to the west of the main body (Della Ceca et al. 1997; Vogler & Pietsch 1997; Bomans et al. 1997). As in the Large Magellanic Cloud, the galaxy NGC 4449 presents a bar–like morphology; it is located at a distance of 3.7 Mpc (Bajaja et al. 1994). NGC4449 is not isolated in the sky; it is a member of the CVn I Cloud which includes a number of Im dwarfs and galaxies such as NGC 4214, NGC 4244 and IC 4182. For a list of relevant parameters, the reader is referred to Table 1.

NGC 4449 shows an unusually rich distribution of blue supergiant stars at its northern periphery (Hunter 1997); this conclusion has been enhanced by ultraviolet (UV) imaging (Hill et al. 1998). The UV results indicate that the UV–emitting populations (OB complexes) lie in the northern part of NGC 4449, while direct propagation of star formation appears possible south of the bar. The latter conclusion was reached using the Hα/FUV(2231Å) ratio, from which age estimations of the OB complexes of this galaxy were derived, indicative of gradients in stellar age. The direct propagation of star formation in NGC 4449 places this galaxy as one of a handful –besides our Galaxy, M82 (Satyapal et al. 1997) and a couple of LMC OB associations and nebulae (Parker et al. 1992; Laval et al. 1992; Rosado et al. 1996)– where sequential star formation has been discerned and measured (Hill et al. 1998).

The morphological and dynamical peculiarities in NGC 4449 are also reflected in its H I and ionized gas contents. The neutral gas in the outer parts of NGC 4449 (van Woerden et al. 1975; Hunter et al. 1998) seems to be counter rotating relative to the ionized gas distributed in the inner disk (Sabbadin et al. 1984; Valdez–Gutiérrez et al. 2000). This counter rotation implies the co–existence of two physical systems rotating in opposite directions in this galaxy. In Irrs, this behavior has only be seen in a few examples: IC 10 (Shostak & Skillman 1989) and NGC 4449 (Sabbadin et al. 1984). As does the LMC, NGC 4449 has a significant magnetic field, a fact which has only recently emerged (Otmianowska–Mazur et al. 2000; Chyży et al. 2000). One of the conclusions reached in these studies is that the existence of a global magnetic field is possible even for small values of galactic rotation ($v_{rot} < 30$ km s^{-1}).

The relatively small distance of NGC 4449 earmarks this specimen for detailed kinematical studies. The first Fabry–Perot (FP) interferometric analysis of this galaxy was performed photographically with a fixed gap FP etalon by Crillon & Monnet (1969), who determined radial velocities for the more prominent complexes of H II regions in a spatial field of 5×5 arcmin. Other researchers who employed scanning FPs to study the kinematics of the gas in NGC 4449 are Malumuth et al. (1986), Arsenault & Roy (1988) and Fuentes-Masip et al. (2000). The observations in Malumuth et al. (1986) were spatially limited (3 arcmin square area) and kinematical interpretations were aggravated due to a loss of parallelism in the etalon plates. Arsenault & Roy (1988) and Fuentes-Masip et al. (2000) focused their work on the study of supersonic velocity dispersions in the brightest H II regions and those H II regions belonging exclusively to the bar. Finally, conventional kinematic studies by means of classic, long slit spectroscopy for NGC 4449 abound in the literature; many projects have been devoted to the most prominent H II regions as well as to the filament and superbubble populations (Sabbadin et al. 1984; Hartmann et al. 1986; Hunter & Gallagher 1997; Martin 1998, and references therein).

In the present analysis, we revisit the analysis of the kinematics of the ionized gas in NGC 4449 as a part of a long term project focused on the study of the interrelationship between gas and stars in irregular galaxies (Valdez–Gutiérrez et al. 2001; Rosado et al. 2001; Borissova et al. 2000, and references therein). This study presents, for the first time, a tridimensional kinematical analysis of the entire, optical distribution of the ionized gas in NGC 4449. Earlier studies had been undertaken by means of longslit spectroscopy and FP interferometry, but focused only on localised objects (such as ionised hydrogen regions) or otherwise, in a smaller field of view compared to the present work.

In Section 2 we describe the FP observations and data reduction. The global, optical morphology in four optical lines are presented in Section 3, as is a statistical analysis of the H II region population. The kinematics of local (H II regions) and global scale features (diffuse ionized gas, global velocity field) are discussed in Section 4. Section 5 is devoted to dynamical results – as deduced from our optical rotation curve. In Section 6 we compare our kinematical results with published H I ones. Finally, in Section 7, we present our conclusions.

2. Observations and Data Reduction

The observations were carried out during four runs with the UNAM Scanning Fabry–Perot interferometer PUMA, attached to the f/7.9 Ritchey–Chrétien focus of the 2.1 m telescope at the Observatorio Astronómico Nacional at San Pedro Mártir, B.C., México. The log of the observations is described in Table 2.

The PUMA setup is composed of a scanning FP interferometer, a focal reducer with a f/3.95 camera, a filter wheel, a calibration system and a Tektronix 1K×1K CCD detector (Rosado et al. 1995). Other components of the instrumental setup used in each run, are the same as described in Table 2 of Valdez–Gutiérrez et al. (2001). Depending on the CCD reading (bin = 1, 2 or 4), the pixel size is $0\farcs58$, $1\farcs17$ or $2\farcs34$, respectively. At our assumed distance (see Table 1), the pixel linear–size is equivalent to 10.5, 21 and 42 pc, respectively. A $10'$ field of view is spanned, embracing the entire optical extent NGC 4449 out to the de Vaucouleurs 25 mag arcsec^{-2} isophote.

We obtained a set of direct images –in three runs– in the lines of Hα, [S II] (λ 6717, 6731 Å), [N II] (λ 6584 Å) and [O III] (λ 5007 Å) using the PUMA in its direct image mode, i.e. without the FP on the optical axis. For their calibration, we have observed, under the same conditions, the spectrophotometric standard star BD+25°3941 (Barnes & Hayes 1982). In the fourth run we exclusively used the Hα filter for direct imaging: see Section 3 and Table 2 for more details of these observations. In the third run, the seeing in the direct images of NGC 4449 – images which were later used to perform our flux calibration– was of the order of $2''$ (FWHM).

In addition, we have obtained scanning FP data cubes in the lines of Hα and [S II]. The FP data cubes are composed of 48 steps covering the entire spectral range, with integration times of 60 seconds per step. In this configuration, the final data cubes had dimensions of 512×512×48 (after applying a binning of two). We have obtained 2 data cubes per filter; the total exposure time was 1.6 hours in each case. The measured seeing in these data cubes is of the order of $2\farcs7$ (FWHM).

FP data reductions (phase calibration and kinematical analysis) were carried out in the same manner as in Valdez–Gutiérrez et al. (2001), mainly using the software package CIGALE (Le Coarer et al. 1993). The photometry was performed under IRAF[6]. Our data cubes in Hα are contaminated with night–sky lines such as the lines of OH at 6568.78 Å and 6568.77 Å. These night–sky lines fall inside the main emission of NGC 4449, centered at channel 14 or at the heliocentric velocity +295 km s^{-1} (in the redshifted wing of single velocity profiles). Such night–sky lines have been subtracted using an interactive routine of CIGALE and consequently our radial velocity dispersions are free of them. The [S II] data cubes are less contaminated by night–sky lines; however, the S/N ratio is not as good as for the Hα cubes and are only used to compare and to complement the Hα observations.

---

[6] IRAF is distributed by the National Optical Astronomy Observatories, operated by the Association of Universities for Research in Astronomy, Inc., under cooperative agreement with the National Science Foundation.

To extract the kinematic information from the FP data cubes, we adopt the same methodology described in Valdez–Gutiérrez et al. (2001). The radial velocity profiles were fitted by Gaussian functions once deconvolved with the instrumental function (an Airy function). We also constructed a set of maps, or moment maps. The first moment is given by the radial velocity map, which CIGALE calculates by finding the barycenter in the radial velocity profile of each pixel. Cleaning this map at 2 σ times the value of the standard background emission, ensures that the remaining features are galactic. The second moment map or the velocity dispersion map, was derived using the Adhoc package (Boulesteix 1993). Besides our moment maps, CIGALE obtained a monochromatic map after integration of the radial velocity profile (velocity versus intensity along the 48 channels) of each pixel, up to a certain fraction of the peak (usually 70%). This map enables us to separate the monochromatic emission from the continuum (Le Coarer et al. 1993).

2.1. Photometric Calibration

To accomplish the flux calibration of our Hα data, the direct images of the standard star BD+25°3941 and the direct images of the galaxy (see previous Section and Table 2 for details) were reduced and analysed in the usual way. In this manner, our conversion factor (to secure absolute calibrated surface brightnesses) was: 1 count s^{-1} pix^{-1} = 1.266×10^{-4} erg cm^{-2} s^{-1} $steradian^{-1}$, which in units of flux is: 1.018×10^{-15} erg cm^{-2} s^{-1}. For images binned by a factor of two, 1 count s^{-1} pix^{-1} corresponds to 3.165×10^{-5} erg cm^{-2} s^{-1} $steradian^{-1}$.

Given that NGC 4449 presents a conspicuous diffuse component pervading almost all of its disk and taking into account that this component is more intense towards the NE–SW bar (Scowen 1992), we considered it appropriate to subtract such diffuse emission only on our direct images, in order to determine the H II region diameters more accurately. For the datacubes, we used another scheme to separate the diffuse emission; that methodology will be explained in the next section.

To subtract the diffuse emission in our Hα direct image of NGC 4449, we used the technique (well known in photometry) of median filtering. In our case, the best filter was that with a square box of 97 pixels. This filter has to be at least 3 times greater (in spatial area) than the most extended feature to be analysed, in order to ensure reliable Hα counts (after subtraction of the filtered image from the direct one). Once the diffuse emission was subtracted, the background was removed at 3 σ of its mean value, to ensure galactic membership of the remaining features. The resulting image is shown in Figure 1. However, some local background persisted, especially at the bar, where the crowding is high. This effect can be seen in our Figure 1 and Figure 7 in Fuentes-Masip et al. (2000).

The next step was to define the H II region boundaries. Later, these were used as apertures from which our photometry was performed. Polygonal apertures were chosen so as to contain all emission from a given H II region (Figure 2). Special care was taken with objects embedded in crowded regions, given that the limits between individual H II regions and the local background were problematic, even when the diffuse emission had been eliminated. In a crowded region (such as the bar) the definition of the apertures was carried out by locally setting a contour map of the complex, to determine the relative contribution of each embedded H II region. Pixels within the apertures were then summed to generate the total area and the total counts for every H II region. The total Hα flux for each H II region was obtained by multiplying the resulting counts by the calibration conversion factor.

Our resulting Hα fluxes for the H II regions are presented in column 4 in Table 3. The uncertainty in the derived fluxes of crowded regions ranges from ±10% for the brightest objects, to 30% for the faintest H II regions. The lowest and highest levels for which we have reliable data in our cataloged H II regions are: 1.9×10^{37} and 3.38×10^{39} erg s^{-1}, respectively; these values correspond to a surface brightness of 6.309×10^{-5} and 1.047×10^{-3}

erg cm^{-2} s^{-1} steradian^{-1}. The lowest value corresponds to our region M92, and the highest one is found in our region M32. The Hα luminosity of the latter region (M32) is approximately 1/5 that of the Hα luminosity for 30 Doradus (1.5×10^{40} erg s^{-1}) and two orders of magnitude brighter than the Orion Nebula –Messier 42, 10^{37} erg s^{-1}, see Kennicutt (1984).

At first glance, it may appear that removal of diffuse emission would help us to assign definite diameters to areas of interest (e.g., ionised hydrogen regions) and hence compute fluxes coming from each such region of interest, but there are complexities, as discussed below.

Our Hα fluxes free of diffuse emission were compared against that obtained by Fuentes-Masip et al. (2000), who also removed the diffuse emission in their work. Fuentes-Masip values resulted in brighter ones than ours, by an amount of ∼60% in the most extreme case, in spite of their diameters being smaller than ours. Also, our best fit to Fuentes-Masip falls on a regression line parallel to the diagonal (slope∼ 0.7). Hence, in order to explore the importance as to whether we should subtract the diffuse emission in the H II region photometry, we compared the fluxes obtained by Hill et al. (1998)(diffuse emission included) against those of Fuentes-Masip (free of diffuse emission). The chosen H II regions were SB89, 108, 114, 133, and 208. The difference in log (L) was 0.6 in the worst case, with the Fuentes-Masip values always brighter than Hill's; recall that Hill's apertures were larger, and had diffuse emission included. In the light of such results, we decided it appropriate to apply our polygonal apertures (defined without diffuse emission) on the monochromatic image (diffuse emission included and transformed to bin=1) and to compute fluxes.

Our flux determinations were compared against published data by Hunter (1982), Scowen (1992) and Fuentes-Masip et al. (2000). The regions chosen to compare were selected from Sabbadin & Bianchini (1979) and Crillon & Monnet (1969) lists. They also were chosen to be relatively isolated, round and intense (especially in the case when a region was embedded in the bar). Figure 3 shows the comparison. In this figure it can be seen that our fluxes are in excellent agreement with those of Hunter (1982), for two bright H II complexes at the bar. Our discrepancies with Scowen (1992) probably are given by the uncertainty in the positions of the apertures. With respect to Fuentes-Masip et al. (2000), our comparison to their values results in a fit with a slope value (b=0.99) parallel to the diagonal, where the Fuentes-Masip values are in general, brighter than ours. The correlation (r∼0.9) found in such fit, is high. This fact points towards the homogeneity in our data and a systematic effect produced by the Fuentes-Masip method of subtracting the diffuse emission and the influence of such effect in the acquisition of their fluxes.

To obtain luminosities, our fluxes were corrected for galactic foreground extinction, even though in the direction of NGC 4449, it is negligible: A$_B$=0.2 mag (de Vaucouleurs et al. 1976; Burstein & Heiles 1978). The effects of internal extinction were not taken into account; they are not crucial in kinematical studies (Hippelein 1986).

2.2. Definition of the Apertures in the FP Data

The H II region apertures –rectangular boxes in this case– in which the kinematical analysis was performed, were assigned using different criteria compared to the scheme followed in the direct imaging mode. The reason is due to the fact that we did not want to apply any filtering technique on our datacubes to eliminate the diffuse emission. This could otherwise introduce a systematic effect over the continuum level at each pixel, as a consequence of such filtering. Therefore, as a first step –as is customary in the analysis of FP data– the boundaries were determined checking all the velocity maps in which emission was detected for a given H II region. In this way, by inspecting each 0.41 Å we were sure that contamination by diffuse emission was not important. Moreover, we only took as 'valid' detections, only those detected in two successive velocity maps.

In order to check if our FP box boundaries were effectively free (and not contaminated) by diffuse emission, we superimposed our FP boxes on the FP monochromatic image in which the H II regions were clearly delineated (such monochromatic images were cleaned of diffuse emission, as previously described in subsection 2.1). We next superimposed our FP boxes on the filtered direct image. The comparison was highly satisfactory; only in some cases did we need to marginally redefine our boxes. For some H II regions embedded in the bar, we secured local contours to examine the relative contribution of the different components and in this way, to assign our box boundaries. The boxes are shown in Section 4.2.

The resulting catalog of kinematic properties (Table 4) differs from that in Table 3; this may be ascribed to different binnings in each case (see Table 2 for details).

3. Global Morphology of the Ionized Gas in NGC 4449

Figure 4 shows the emission of NGC 4449 in the lines of Hα, [S II], [N II] and [O III] as obtained from our direct images in the second run (see Section 2 and Table 2 for more details). In these images it can be seen that the dimensions of the galaxy's main body –at the adopted distance– are approximately $4\rlap{.}'4$ or 4.8 kpc and $2\rlap{.}'7$ or 3 kpc for its major and minor axes (not shown), respectively. Seen at these large scales, the Hα and [O III] global emission of NGC 4449 appears to be mainly concentrated toward the south, where copious numbers of H II region complexes, superbubbles and filaments are found. However, the presence of filaments and superbubbles is not related exclusively to the main body: an "arc" of emission is visible at the west from the photometric center as far as $2\rlap{.}'6$ or 2.8 kpc. Such a feature is referred to in other works as arc 156–157 (Scowen 1992) or SGS3 (Bomans et al. 1997), and it is better seen in Hα and [S II].

The most prominent spatial extent of emission NGC 4449 is located, in projection, along the bright bar – which extends from NE to SW and whose morphology is conspicuous in all the filters. Along the bar lies a hugely strong continuum whose location corresponds to the photometric center. This feature has been referred to as a "nucleus" and its nature has been recently analysed by Böker et al. (2001) and Gelatt et al. (2001). The results of these works points towards the existence of a young super star–cluster embedded at that location: a fact which is possibly related to the previous interactions suffered by this galaxy. Moreover, the bar possesses a pervasive diffuse ionized gas component. This diffuse gas also embraces almost the entire optical extent of the galaxy, as we have already alluded to.

To the north of NGC 4449, the bright complexes CM46 and CM39 (Crillon & Monnet 1969) emit more strongly in Hα, [S II] and [O III] compared to [N II], where they look dimmer. The SNR previously reported (Seaquist & Bignell 1978; Balick & Heckman 1978, also known as H II region SB187) is located in our images at the SW border of our region M77 or V61 (see Tables 3 and 4) and appears brighter in [O III] than in Hα. In our region M77(V61) the H II regions SB185 and SB187 (Sabbadin & Bianchini 1979) look almost blended and embedded in a diffuse emitting region. At the borders of this H II complex, the presence of the superbubble SB2 (Bomans et al. 1997) or NGC 4449–D (Martin 1998) is unmistakable as suggested by the complexity of the radial velocity field at that locale. Apart from the features above, the galaxy appears to have a fuzzy morphology in the lines of [S II] and [N II], given that the continuum has not been subtracted. Nevertheless, the bar remains as the most distinct feature in contrast to other regions with negligible emission.

As far as the beautiful and sprawling filaments are concerned, these emerge in the Hα and [O III] filter images at first glance, as opposed through the [S II] and [N II] filters, where they are not well discerned (mainly due to the diffuse emission). Filament 6 (Hunter & Gallagher 1997) and the bulk of filaments already reported (Bomans et al. 1997, and references therein), are indeed prominent in our Hα direct image. In the [O III] image, the number of resolved filaments (Bomans et al. 1997) is less, but filament 6 remains resolved.

We also have conducted Hα direct observations around the locations where some H I maxima have been reported (Hunter et al. 1998). Information pertaining to this run is displayed in Tables 2 and 5. In Table 2, the corresponding frames are indicated with positions 1, 2 and 3. Our goal was to look for traces of star formation at those locales. However, we did not find obvious Hα emission at these three positions, although we performed an unsharp masking treatment in our images. This result agrees with the work of Hunter et al. (2000b) for positions 2 and 3. At our position 1, there are no other published comparisons pertaining to the issue of star formation there.

3.1. The H II Region Population

The H II regions of NGC 4449 have been catalogued by Crillon & Monnet (1969), Hodge (1969), Sabbadin & Bianchini (1979) and Hodge & Kennicutt (1983). The most extensive catalogue corresponds to Sabbadin & Bianchini (1979) with 252 regions. Our identifications are mainly based on this work and on the earlier work of Hodge (1969).

Our observations contain 140 H II regions according to Sabbadin & Bianchini (1979). Two other regions not catalogued in this work are denoted in the second column of Table 3 and Table 4, and demarcated as h61 and h66 according to Hodge (1969). Futhermore, regions denoted by a "V" letter followed by a number in column 2 of Table 3, correspond to our sources listed in Table 4. The ionised hydrogen regions detected by Sabbadin & Bianchini (1979) but not by us is due to several possibilities: very weak emission (and consequently not detected by us); alternatively, some were possibly not resolved with our telescopic and FP configuration. Another issue is blending: in some cases, the boundaries between diffuse H II regions being part of one large complex were not obvious. In such cases, we assigned them with a common boundary. Taking into account all these scenarios, only 84 and 101 regions were cleanly defined in our monochromatic and direct images respectively.

Table 3 shows the results of our photometry performed on the H II regions in NGC 4449. Columns 1 and 2 present the identifications of each source in this work and in previous ones (Hodge 1969; Sabbadin & Bianchini 1979, and this work). Column 3 shows the equivalent diameter (D), which is defined in terms of the area (A) where the photometry is performed: A= $\pi(\mathrm{D}/2)^2$. Column 4 displays the logarithm of the Hα flux, derived as described in Section 2.1. Finally, columns 5 and 6 show the luminosities and surface brightnesses.

3.2. The H II Region Luminosity Function

Figure 5 shows the Hα luminosity function for the H II regions in NGC 4449. For several galaxies, it has been shown that the brighter luminosity end of the H II region luminosity function can be fitted with a power law in the form: $N(L)$=AL^a dL , where N is the number of H II regions with luminosity L in an interval of luminosity dL, and the slope a is related to the morphological type of the galaxy (Kennicutt et al. 1989), ranging from mean values of −2.3 (Sab–Sb galaxies) to −1.75 (Irrs). It also has been suggested that different ranges of the luminosity function are related to different kind of objects such as H II regions ionized by single stars compared to those ionized by clusters of stars (Hodge et al. 1989; Youngblood & Hunter 1999).

In order to obtain the H II region luminosity function, we followed the procedure already described in Valdez–Gutiérrez et al. (2001). For NGC 4449 the bin width was more refined than in Valdez–Gutiérrez et al. (2001, with 30 H II regions), and the fit was calculated in bins brighter than $\log L = 38.6$, showing a negative slope.Composite regions as M87 or M90, were excluded in the fit. Our best fit slope for NGC 4449 gives $a = -1.93 \pm 0.2$. This value is in good agreement (within our error bars) with the value ($a = -1.9$) found by Fuentes-Masip et al. (2000), and lie within the errors of the mean values found for a sample of Irr galaxies studied by Kennicutt et al. (1989), Strobel et al. (1991), Kingsburgh & McCall (1998) and Youngblood & Hunter (1999). These studies were performed on six, three, twenty–nine and four Irr galaxies respectively; only the work by Kennicutt et al. includes NGC 4449.

3.3. The H II Region Diameter Distribution

The H II region diameter distribution can be expressed as: $N(> D)$=N_0 $\exp(-D/D_0)$, where $N(> D)$ is the cumulative function of H II regions with diameter larger than D, and D_0 is the characteristic diameter. This functional dependence was proposed by van den Bergh (1981) as an universal law for all galaxy types and it has been used to study the statistics of the H II region populations in combination with the H II region luminosity function. However, in a recent work (Pleuss et al. 2000), there appears to be a dependence of the slope in the distribution function with respect to the spatial resolution. Thus, care has to be taken with regard to values in slope whose resolution data lies under 40 pc FWHM (Pleuss et al. 2000).

To calculate the distribution we have used the diameters of the H II regions measured on the direct Hα images; these are to be found in column 3 in Table 3. According to our definition, the equivalent diameters range from 38.8 pc (corresponding to our region M41) to 184.4 pc (for region M32), with a mean value of 89.1±31.6 pc. Our mean diameter value is in agreement (within dispersion values and within adopted distance uncertainties) with a mean value previously reported (Fuentes-Masip et al. 2000). Recall that the latter study considers only 43 regions and that it also takes into account the subtraction of the diffuse emission in the determination of diameters. On the other hand, the large dispersion found in our mean equivalent diameter accounts for the wide range in the sizes of the H II regions in this galaxy.

The resulting cumulative H II region diameter distribution $N(>D)$ is shown in Figure 6, where we plot $\log N(>D)\, vs\, D$. For NGC 4449 a least squares fit gives D_0 $=1\rlap{.}''73$±0.1 or 31.2±2.1 pc. In the calculation we have included the diameters of H II complexes –not ring shaped– which envelop more than one region. This value is in agreement with a previously published value by Fuentes-Masip et al. (2000) who obtained D_0=$1\rlap{.}''6$. However, our value differs from that of Hodge (1983) and Sabbadin & Bianchini (1979) who quoted larger values: D_0= $5\rlap{.}''5$ and $6\rlap{.}''2$, respectively. The disagreement here could possibly be due to the diffuse emission not being subtracted in these studies. To this end, Pleuss et al. (2000) suggest that the intrinsic clustering properties of the H II regions plus diffuse emission and resolution effects, do indeed hamper reliable measurements of internal quantities (such as luminosities and diameters).

Pertaining to the correlation between D_0 and the absolute magnitude M_B given by Strobel et al. (1991):

$$\log D_0 = 0.25(\pm 0.29) - 0.098(\pm 0.017) M_B,$$

when we plot our observational value ($\log D_0 = 1.5$) as well as the resulting value from the above equation, $\log D_0 = 2.06 \pm 0.3$, taking $M_B = -18.5$ (Schmidt & Boller 1992), the first value does not fit the correlation in Figure 11 in Strobel et al. (1991), while the latter does. This supports the conclusion of Strobel et al. (1991) and Youngblood & Hunter (1999), who analyzed a sample of 29 Irrs (NGC 4449 not included) and Blue Compact Dwarfs, and who highlighted the weakness of this correlation.

4. Kinematical Analysis on Global and Local Scales

4.1. The Global Velocity Field of NGC 4449

In NGC 4449 we detected Hα emission ranging from 75 to 472 km s^{-1} in heliocentric radial velocities; some velocity channels are displayed in Figure 7. Also, the global radial velocity profiles for all emission emanating from this galaxy has been fitted. The results are displayed in Figure 8. In this figure one can immediately see that the peak velocity of the whole emission is at channel 10.5 (or 218 ± 4 km s^{-1}) with a corrected velocity dispersion of 1.7 channels (or 31.5 ± 10 km s^{-1}). The other curves in that Figure correspond to sky–line fittings; curve 3 contributes to the profile in our line under study (Hα), and it has been taken into account in all calculations determining radial velocities and velocity dispersions. The peak velocity can be considered the systemic velocity of the galaxy, and the velocity dispersion can be visualized as the representative value of the velocity dispersion of all the objects embedded in the disk. At this point, we do however caution that Hα velocity dispersions are subject to many factors which contribute to its broadening. In this sense, a better velocity dispersion determination can be derived from other forbidden lines. However, given the low metallicity of Irrs as a class, the Hα line is invariably adopted in FP studies (such as this one) due to its relatively high intensity.

Figure 9 (top and bottom left) shows the global radial velocity field of NGC 4449 obtained from all the detected Hα emission: H II regions, bubbles, filaments, as well as the diffuse emission. Along the bar going to the SW, a conspicuous gradual decrement in radial velocities can be noticed ranging from approximately 250 km s^{-1} in the NE to $\sim$ 190 km s^{-1} in the SW. This result is in excellent agreement when it is compared against previous works (Crillon & Monnet 1969; Sabbadin et al. 1984; Malumuth et al. 1986; Yoshida et al. 1995). We are able to conclude that the gradient in radial velocities of the H II gas is indeed in the opposite sense compared to the outer H I distribution, as was reported in an earlier study by van Woerden et al. (1975) from H I studies, and Sabbadin et al. (1984) from Hα ones.

Figure 9 (bottom right) displays the global velocity dispersion field (corrected as indicated in Section 4.2). As can be seen, NGC 4449 presents low velocity dispersion values at its eastern and western sides, no larger than 25 km s^{-1}. However, the velocity dispersion values increases as one moves towards the interior of the galaxy, reaching 40 km s^{-1}. The extreme values occur at the SNR location, as well as at some places along the bar, with values in a range of 45–60 km s^{-1}. Our results along the bar are in good agreement with the velocity dispersion map presented by Fuentes-Masip et al. (2000), and in disagreement with Malumuth et al. (1986), who obtained larger values (by about a factor of two) at the same locations. The latter authors may have precluded the signifance of a loss of parallelism in their FP plates.

The recession velocity of the nucleus (which has been indicated with a cross in Figure 10) is 220 ± 4 km s^{-1}, in excellent agreement according to Sabbadin et al. (1984, 223 ± 5 km s^{-1}) and within the errors published in Fouque et al. (1992, 216 ± 28 km s^{-1}). With respect to our [S II] data cubes, we generally find a good agreement (where the signal/noise was high enough) with other Hα radial velocity studies cited earlier in this paper.

4.1.1. Local Superimposed Motions

Besides the NE–SW velocity decrement in radial velocities, an intruiging substructure appears in our map: two ring–like structures (one of them located at the NW of the galaxy and embracing our regions V74 and V75; the other structure located at the north end of the bar enclosing our regions V18, V34, V49 and V53) are seen. Such structures are noticeable in Figure 9 (top and bottom left) and are comprised of both H II regions as well as diffuse emission. When one studies the H II regions alone –Figure 9 (top right)– we note that such structures are not so apparent. We actually find a spatial correspondence of the the second ring (described above) with a peculiar behavior of the magnetic vectors at this location. In Figure 3 of Chyży et al. (2000), a divergence in the polarization vectors occurs at low values (sometimes actually reaching zero), at this ring–like structure. As the optical radial velocity field is somewhat chaotic at this locale, it may be expected that magnetic fields do, to some degree, trace such gas kinematics (Beck and Urbanik, priv. comm.).

Furthermore, in Figure 9 (top and bottom left) we find superbubbles, filaments and giant H II complexes which have also been observed in previous studies (Hunter & Gallagher 1997; Bomans et al. 1997). As far as the giant filament 6 (Hunter & Gallagher 1992) is concerned, we are able to only see it when spatial filtering was applied to our monochromatic chart. More details of our analysis in this filament and in other filaments –as well as detailed results about the superbubble and SNR populations– will be given in a forthcoming paper (Valdez–Gutiérrez et al. 2003, in preparation).

Extreme values in detected velocities (such as those arising from the internal motions of the superbubble, SNR and filament populations) may not properly be deduced in our Figure 9 since we selected our palette to enhance the velocity gradient along the major axis. However, as discussed in the next section, when the kinematics of these populations are analysed in detail, a complex and rather chaotic behavior emerges. In our map, there are some regions where abrupt radial velocity gradients appear: for example, at the north end of the bar –where there are some clues that some superbubbles are blending– and at the location of the superluminous SNR. Indeed, at the latter zone there is an H I hole and the filaments 5 and 6 reported by Hunter & Gallagher (1992) lie at the borders of an H I ridge.

In the surrounding velocity field outside of the bar, we find regions characterized by both large radial velocities and high velocity dispersions (details in the next section), in accord with Malumuth et al. (1986). Such locations are places where filaments and superbubbles have been reported (Scowen 1992; Bomans et al. 1997; Martin 1998).

To explore this farther, we have analysed the radial velocity field at the seven locations where Malumuth et al. (1986) report strong radial velocity gradients (see their Figure 6 and our Figure 11 top right). After a detailed kinematical analysis –employing profile decompositions at those locales– our results agree qualitatively with Malumuth's and with our values reported for the diffuse ionized component (see below). We also find that the seven Malumuth's regions are coincident (at least in projection) with filaments or superbubbles. Due to the presence of such objects, the scenario proposed by Hartmann et al. (1986) in which gas cloud infall is generating such kinematics, could possibly be discarded. However, in order to elucidate the origin of the local, steep radial velocity gradients at the above mentioned locations, detailed kinematical studies have to be performed. With respect to the velocity field at those locales where Hill et al. (1998, see their Figure 14) postulated that star formation propagated in a stochastic manner, we find that the radial velocity profiles there are often complex, admitting more than one component (as can be seen in our Table 4). Such locations spatially correspond to regimes where H II complexes, filaments and bubbles are seen in projection.

We have already noted that the global velocity field in NGC 4449 is moderately well behaved, but becomes increasingly chaotic as one considers smaller scales (as discussed in the the sections which follow). Also, the projected borders of the bar exhibits abrupt gradients in radial velocity and in velocity dispersion. What we therefore encountering here in the optical inner part of NGC 4449 is a highly perturbed medium due to an intense star forming rate – high compared to other Irrs (Hunter et al. 1999). The star formation rate in this galaxy is undoubtedly enhanced by bar–like gravitational well. We strongly believe that all of these kinematical and dynamical features suggest a prior encounter of this galaxy with the Irr DDO 125. This scenario was proposed by Hunter et al. (1998) based on H I data covering a spatial extent of about $67' \times 67'$. Later, Theis & Kohle (2001) performed numerical simulations which reinforced such a scenario.

4.2. Kinematics of the H II Regions in NGC 4449

Figure 10 shows the Hα monochromatic image of NGC 4449 (continuum subtracted) obtained from our FP cubes using the method described in Section 2. Superimposed on this image are the rectangular boxes (see Section 2.2) from which the radial velocity measurements of the observed H II regions have been computed. We obtained the radial velocity profiles of these sources by integrating within these rectangular boxes. We will refer to these profiles as “integrated” because they are obtained by integrating over the whole extent of the H II region. We also mark the position of the SNR with a filled circle.

In general, one single Gaussian function may be used for fitting the integrated radial velocity profiles. Only in five cases (V34, V56, V64, V65 and V76) are the integrated velocity profiles more complex. In these cases, we carried out a profile decomposition using two Gaussian functions. In these cases, we list the second velocity components (obtained from our profile fitting) in columns 4 and 6 of Table 4.

Table 4 catalogues the kinematics of the H II regions throughout the optical extent of NGC 4449 spanned by our observations. We have labeled each region V1, V2, ... in column 1; cross identification of these regions in previously published papers are listed in column 2; the peak velocity is listed in columns 3 and 4; velocity dispersion values (from fitting a Gaussian to the radial velocity profiles) may be found in columns 5 and 6. Column 7 lists young stellar groups associated with our regions V1, V2, ... while comments on the sources appear in column 8. In these comments, “a” denotes asymmetric profiles, while “s” demarcates symmetric ones.

The radial velocities were corrected to the heliocentric system of reference. Our observational velocity dispersions (σ_{obs} = FWHM$_{obs}$/2.354) have been corrected for instrumental (σ_{inst}), thermal (σ_{th}) and intrinsic (σ_{intrin}) broadenings, according to:

$$\sigma^2_{corr} = \sigma^2_{obs} - \sigma^2_{inst} - \sigma^2_{th} - \sigma^2_{intrin}$$

where σ_{inst} = 21.7 km s^{-1}, σ_{th} = 9.1 km s^{-1} for hydrogen gas at T$_e$=10^4 (Spitzer 1978) and σ_{intrin} = 3 km s^{-1} for the fine structure of the Hα line. The resulting σ_{corr} is also referred as the turbulent velocity dispersion by some authors. The accuracy in the determination of peak velocities as well as error determinations in the fitting of radial heliocentric velocities and velocity dispersions related to PUMA data, have been previously reported in Rosado et al. (2001).

As can be seen in this Table, the H II region heliocentric radial velocities (of single profiles) range from 183 (source V22) to 254 km s^{-1} (source V13). Within errors, these values are in agreement with previously published values (Crillon & Monnet 1969; Sabbadin et al. 1984; Malumuth et al. 1986). When compared to the study of Fuentes-Masip et al. (2000), our radial velocities show a tendency to be universally lower. By means of a least squares fit, the best slope value to Fuentes-Masip velocities is 0.74±0.07 with a correlation coefficient of 0.9; the amount of the difference reaches 14 km s^{-1} in the most extreme cases.

On the other hand, some extreme velocities were detected in regions with composite profiles: their velocity ranges from 185 (source V65) to 352 km s^{-1} (source V34). Inspecting our velocity charts, the objects related to these velocities are identified as H II regions coinciding (in projection) with filaments discovered by Sabbadin & Bianchini (1979), Scowen (1992), Hunter & Gallagher (1997), Bomans et al. (1997) and Martin (1998).

The corrected velocity dispersions are supersonic for most of the objects, with values ranging from 11.8 to 37.4 km s^{-1} with a mean value of 22.8 km s^{-1}. This is in agreement with Fuentes-Masip et al. 2000 who measured 44 H II regions belonging exclusively to the bar. Some relatively isolated H II regions or H II regions being part of a complex, had low S/N ratios and consequently the determinations of peak velocity and velocity dispersion were uncertain. Such cases are marked with a "u" in column 2 of Table 4.

Young stars related to our H II regions are indicated in Column 7 of Table 4. Such information is based on a previous study by Hill et al. (1998). Hill et al. (1998) identified the locale of OB associations (as well as complexes of OB associations) using ratios of far ultraviolet (FUV) and optical imaging. In that analysis, OB associations and OB complexes were studied by defining 'small' and 'large' apertures, respectively. Column 7 of Table 4 indicates the young stellar content according to the work of Hill et al. (1998): a number followed by a capital letter refers to a 'large' aperture while stand–alone numbers indicates the use of 'small' apertures (see Tables 5 and 8 in Hill et al. 1988). In that column, a blank space means that there is no indication of a young stellar population in Hill's data, or that some of our regions were not covered by their observations. In general, the most notable complexes show a spatial correlation with young stellar associations. Future studies with better resolution and sensitivity at both wavelengths (than those available to Hill et al. 1998) will undoubtedly provide further insight here.

4.3. Kinematics of the Diffuse Ionized Gas in NGC 4449

We have already noted that NGC 4449 presents a diffuse, ionized gaseous component which permeates almost the entire optical extent of the galaxy. The nature of the diffuse ionized gas –also called DIG or warm ionized medium (WIM)– which is found in the form of shells, loops, and a widespread unstructured diffuse background, has become a field of intense research. Review papers may be found in Reynolds (1991, 1993).

In view of the fact that our observations covered the optical disk of NGC 4449, we performed a detailed analysis of the properties of its extended DIG (i.e. the widespread diffuse background). Contrary to what we find in the Local Group Irr IC 1613 (Valdez–Gutiérrez et al. 2001), the DIG in NGC4449 is more turbulent and reflects the influence of its activity at local scales (see below) and at global scales (see next section).

Concerning DIG photometric properties in NGC 4449, we find a gradual increment in surface brightness values as one moves from the outskirts of the galaxy towards the inner regions (see Figure 11, top left). In this way, surface brightness values at the outlying periphery of NGC 4449 range from 3.165×10^{-5} to 2.215×10^{-4} erg cm^{-2} s^{-1} $steradian^{-1}$ (or $4.17\times10^{35} - 2.91\times10^{36}$ erg s^{-1} in luminosity units) at the inner regions surrounding the brightest H II complexes. These values are approximately smaller by a factor of four than those found by Fuentes-Masip et al. (2000, see their Figure 2) in the diffuse gas at the bar locations. However, our values found for the DIG in the outer extremities of the disk correspond well with those found by Hunter & Gallagher (1990) at the locations of two loops along the bar. The corresponding emission of the outlying DIG is $EM \sim 280$ cm^{-6} pc, which falls in the range obtained by Hunter & Gallagher (1990).

We also compute the total DIG luminosity in NGC 4449. The DIG luminosity we find is 5.49×10^{39} erg sec^{-1} (or 3.35×10^{-12} erg cm^{-2} sec^{-1}), which is ∼10% the total Hα luminosity reported by Hunter et al. (1999). Previous measurements of the DIG fraction in this galaxy (Hunter & Gallagher 1990) report a range of 15–20% of the total Hα luminosity. The disagreement with our value undoubtedly resides in the deeper observations performed by Hunter and collaborators. In the Large Magellanic Cloud, the DIG contribution is estimated to be about 15–25% of the total Hα flux (Kennicutt & Hodge 1986). These values are very small compared to the DIG luminosity in some spirals, which may amount to 30% or even 50% of the total Hα luminosity (Ferguson et al. 1996).

The kinematics of the DIG is displayed (according to the entire spatial distribution) in Figure 11 (top right). We show there the DIG's radial velocity field. To compute this, the H II regions were subtracted from the whole field (the procedure was explained earlier, in Section 2.1). In this map, a decreasing gradient of radial velocities from NE to SW can be noted, which follows the tendency already seen in the total ionized gas content (H II regions plus DIG; see previous sections), and in agreement with previous results (Section 4.1). Locally, part of the ring–like structure (discussed in Section 4.1.1), can barely be disentangled at the north end of the bar. With respect to the velocity dispersion in the widespread DIG, we find an increment in their values, from the peripheral optical domains of NGC 4449, towards the interior of the disk. The total displayed range in velocity dispersion is $\sim$70 km s^{-1}, varying from around 10 km s^{-1} to $\sim$75 km s^{-1}. The maximum value we detected lay at the east of our region V65 (see Figure 10). Moreover, values larger than 50 km s^{-1} were also found east of the bar (between our regions V41, V42 and V52), as well as west of the nucleus. The latter locales lie close to our boxes V56, V83, V84; also at the NE sector of the bar (between our regions V33, V47 and V30), and at the vicinities of the SNR (surrounding our region V55).

In order to quantitatively analyse the kinematical properties in the widespread DIG in NGC 4449, we performed a profile decomposition at a few locations. The DIG radial velocity map displayed in Figure 11 (top right), was used to define boxes at different positions of interest. We then performed a profile decomposition within such boxes, as in section 4.2. In this way, we could then secure kinematical properties of the DIG in terms of heliocentric radial velocities and corrected velocity dispersions. The zones which displayed very peculiar profiles were those surrounding the bar, coinciding in many cases with regions where Malumuth et al. (1986) suggested a gas infall. Their positions are indicated in Figure 11. These locales coincide –at least in projection– with positions where filaments or shells have been reported (Hunter & Gallagher 1992; Scowen 1992; Bomans et al. 1997; Martin 1998). Characteristic of NGC 4449 is its network of filaments, loops, shells, and the like. Pertaining to the profile decomposition we performed at Malumuth's locations (see their Figure 6), we are confident they indeed are representative of the profiles at any location in the pervasive DIG of NGC 4449. Some examples of typical profiles we find at four of the Malumuth et al. (1986) locations are shown in Figure 12.

In general, the DIG profiles are very complex (multi–component fits required per profile) at almost all locations. The main component in these profiles always retained values of $\pm$23 km s^{-1} from the systemic velocity (220$\pm$4 km s^{-1}). Beside this main component, we find blue and red components: the blue one having a range of 117 to 144 km s^{-1} while the red component ranged from 275 to 332 km s^{-1}. With respect to the velocity dispersions, the DIG values in the main component reaches up to four times the velocity dispersion of the nearest H II region (see box 3, which is spatially in contact with regions V60, V64 and V65). The resulting DIG velocities and velocity dispersions were larger than the values we secured for the H II regions closest to the DIG boxes. We do however caution that fits to more than one component at such locations are to be treated carefully, given high perturbations in the velocity field (as already alluded to in our previous discussions).

From our results of the global DIG maps (both in radial velocity and in velocity dispersion; see Figure 11) as well as from our profile decomposition, we find that some locations inside the widespread DIG in NGC 4449 show a truly chaotic kinematical behavior. It is tempting to postulate that some of the DIG locations we analysed have, as a source of their fueling, energetic photons escaping from H II complexes. Of course for the very widespread DIG over the disk of NGC4449, any inference with star forming regions and DIG is, at best, indirect.

Let us reflect back on the dynamical history of NGC 4449. After a likely interaction with the Irr DDO 125, (Hunter et al. 1998; Theis & Kohle 2001) a bar potential took form, in which gaseous infall and star formation is taking place on a highly efficient basis (Malumuth et al. 1986). Other secondary manifestations (aftermaths of the interaction) could be the loops, shells, filaments, etc: clear signatures of the highly perturbed velocity field. Indeed, a past interaction experienced by NGC 4449 could be the crucial factor as to why the ISM in this galaxy is so active and peculiar.

5. The Optical Rotation Curve of NGC 4449

Given that we have kinematical data for the ionized gas spanning the entire optical disk, the next step is obviously to derive the rotation curve. However, we must point out that irregular galaxies invariably show low rotation velocities because of their low masses.

For NGC 4449, we calculate the rotation curve using the radial velocities resulting from our FP cubes. First, we use the first moment map or radial velocity chart, and we apply a mask. The mask is constructed using the monochromatic map previously cleaned at 3σ times the mean value of the background. In this way, we obtain a radial velocity field with non–zero values in the positions where there is Hα emission. We then calculate the rotation curve by using the classical formulae, as follows:

$$\Theta(R_k) = \frac{v_k - v_0}{\cos\theta_k \sin i}$$

where $\Theta(R_k)$ is the rotation velocity at the position R_k, v_k is the heliocentric radial velocity at that position, v_0 is the systemic velocity, θ_k is the azimuthal position of the data point, and i is the inclination of the galaxy (Mihalas & Binney 1981). This formulae assumes that the major axis is oriented at $\theta = 0°$.

We have developed a program which calculates the rotation curve once the central pixel, the systemic velocity, and the position and inclination angles (only points in ±20° around the major axis are specified). We compute the difference between the receding and approaching portions of the disk at any galactocentric radius. While this method works well for spiral galaxies, caution should be exercised in the case of irregulars, with their low rotation velocities and their intrinsic disk asymmetries.

For this galaxy, the dynamical center is assumed to lie at RA(2000)=$12^{\mathrm{h}}28^{\mathrm{m}}14.7^{\mathrm{s}}$ and Dec(2000)=$44°05'30''$ (which coincides with the photometric center). Contrary to what has been found for the LMC – where there is an offset between the optical center and the HI dynamical center (Kim et al. 1998) – in NGC 4449, both optical and HI centres spatially coincide (Hunter et al. 1999). We adopt $v_0 = 217$ km sec^{-1}, $PA = 25°$ and $i = 43°$. Comparing the computed values with those in other papers, our v_0 is in agreement with the value determined by Bajaja et al. (1994).

Regarding the PA, our choice for this value disagrees with the value given in the RC3 catalog (de Vaucouleurs et al. 1991); We recall that RC3 values are determined from optical Population I morphologies. In a recent work (Hunter et al. 1999), it is noted that the PA (in the Population I component) rotates E from N as the radius increases, indicative of the presence of a stellar bar potential. Thus, the disagreement of our PA with that in RC3 might conceivably be due to the fact that in this study we are exclusively dealing with the ionized gas component. Finally, our inclination (i) agrees extremely well with Tully (1988).

The resulting rotation curve is shown in Figure 13. From this Figure we can see that the gas in this galaxy rotates slowly around the bar perturbation with a maximum velocity value of ~ 40 km s^{-1} at a radius of 2 kpc in the NE; on the contrary, the rotation curve displays substantial velocity gradients at the SW zone.

It should be noted that the NE side of the galaxy (the receding side) shows a smooth behavior which can be fitted by solid body rotation. In contrast, the approaching side is less populated with H II regions and the results are quite chaotic on local scales. Given the likely scenario of NGC 4449 having undergone an interaction in the past (Hartmann et al. 1986; Hunter et al. 1998; Kohle 1999; Theis 1999; Theis & Kohle 2001), the highly perturbed radial velocity field in approaching side may bear some former signature of the interaction with DDO 125 (Hunter et al. 1998).

When we compare our results with the H I rotation curve calculated by Martin (1998), the agreement is good to within 30% of the measured values (she reports 30 km s^{-1} at 2 kpc). From optical studies, Malumuth et al. (1986) report a *line–of–sight* rotation velocity of 15 km s^{-1} in the bar. In this case, our velocity map in Figure 9 displays a *line–of–sight* rotation velocity of around $\sim$ 20 km s^{-1}. Taking into account our uncertainties –see Rosado et al. (2001) – the agreement is good.

Using our derived optical rotation curve, we calculate the mass inside the limiting radius reached by our observations. Taking the receding side in our rotation curve, the mass inside the optical radius of about 2 kpc, is 7.2×10^8 $M_\odot$. This result is in agreement with the optical mass derived in a previous work (Theis & Kohle 2001). Using our derived mass value, we determine the central density in NGC 4449; we derive a value ρ= 0.021 $M_\odot$ pc^{-3}. This value is in excellent agreement with the average value $\rho_c = 0.02$ $M_\odot$ pc^{-3}, recently found for galactic halo central densities (Firmani et al. 2000, 2001). It is interesting to note that the central halo densities are almost independent of galactic mass –whether dealing on galactic or galaxy cluster scales– in frameworks of cold dark matter cosmologies.

In summary, we quantitatively find that the ionized gas in NGC 4449 is rotating weakly, as has been suggested previously (Sabbadin et al. 1984; Hartmann et al. 1986). However, solid body rotation is only applicable for the NE sector of the disk. The SW side demonstrates abrupt radial velocity gradients, with differences greater than 100 km s^{-1} for regions practically in contact (at least in projection). Due to substantial uncertainties in many of our data points at those SW locations, we did not deem it fit to determine the nature of the SW side rotation pattern in any further detail than explored here.

6. Comparison Against the H I Component

NGC 4449 has been recently studied in the H I content by Hunter et al. (1999). The spatial and velocity resolution in that analysis was $9\farcs8 \times 7\farcs78$ and 10 km s^{-1}, respectively. In our discussion here, we focus on the H I component which spatially corresponds with our optical observations (Figures 14 and 16 in Hunter et al. 1999).

In the optical body of the galaxy, the H I velocity field follows the behavior which we determined for the ionized gas (compare our Figure 9 with Figure 14 in Hunter et al. 1999). In the NE side of the optical body, the H I velocity field presents values of the order of 240 km s^{-1}, while it decreases in the SW sector, to values of order 190 km s^{-1}. As one approaches the outermost detected peripheries in the H I distribution (inside the inner $13\farcs4$), the velocity field is rather complex. Farther to the SW, the H I velocity field increases in value (up to 350–400 km s^{-1}). This also includes the locale of the “arc” (west of the photometric center) already described in Section 3. On the other hand, going farther to the NE, the H I velocity field decreases to values of 150–190 km s^{-1}. The outer H I counterrotates relative to the inner H I. The complex behavior shown by the H I velocity field is probably a result of the interaction between NGC 4449 and DDO 125 (Theis & Kohle 2001).

The H I velocity dispersions inside the limits of the optical disk are of the order of 15–35 km s^{-1}. Along the optical bar, the highest values (25–27 km s^{-1}) correspond to three locales, as also found in this work and by Malumuth et al. (1986). Going to the NE end of the bar, the velocity dispersions experience an increment in their values, reaching 35 km s^{-1} around the location where we report a ring–like feature (section 4.1.1), encircled by regions V25, V31, V34, and V48. For the remainder of the northern sector of the disk, the velocity dispersions lie in the range of 12.5–20 km s^{-1}. In the optical disk, the H I velocity dispersion field shows the same behavior we calculated with our FP data. The main difference is that the ionized gas presents higher velocity dispersions – of order 2 times those in H I (compare our Figure 9 with Figure 16 in Hunter et al. 1999).

This galaxy clearly does not present a classical picture of a symmetric global velocity field in H I; most likely again due to the interloper DDO 125 (Hunter et al. 1998; Theis & Kohle 2001). The H I column density distribution also betrays hints of a past interaction. The peak of the H I column density is located far away from the optical center, at a distance of approximately 50″, which corresponds to 900 pc. Also, as noted by Hunter et al. (1999), there is little detailed correlation between the column density of the H I gas and the presence of H II regions.

7. Conclusions

We have successfully performed a detailed kinematical and dynamical analysis of the entire ionized gas content in the nearby irregular galaxy NGC 4449, by means of Fabry–Perot interferometry. The analysis has been accomplished separately on both global as well as local scales and several of our conclusions are new.

On local scales, we focused our attention on the H II region population, extracting radial velocities and velocity dispersions. In this way, we present, for the first time, the most extensive kinematical catalog of the H II regions in this galaxy yet published. We find that the H II region population shows similar integrated properties when compared to kinematical data previously obtained in the relatively isolated irregular IC 1613 (Valdez–Gutiérrez et al. 2001). The latter statement also applies to the velocity dispersions in the star forming regions: in both galaxies, they are approximately identical. Moreover, in many cases we did detected velocity profiles indicative of a complex structure not fitted by *single* gaussian curves. These profiles are undoubtedly related to the high perturbed radial velocity field, which shows traces of a plethora of superbubbles, filaments and a very active (and widespread) diffuse ionized gas spanning the entire optical disk. Statistically, using the H II region diameter distribution and the H II region luminosity function, we find that the star forming complexes are typical of those obtained for larger samples of irregulars.

We furthermore analysed the kinematical properties of the diffuse ionized gas (DIG) on global scales by means of radial velocity and velocity dispersion fields; locally, we explored the kinematics, making use of profile decomposition. As far as we are aware, this is the first time that such an analysis has been performed in this object. Our results point towards a highly chaotic medium, especially at those locations close to the brightest H II complexes in the bar. We postulate that the chaotic radial velocity field induces local compression ensuring the propagation of stochastic star formation –as also discussed by Hartmann et al. (1986).

On global scales, we find a relatively well behaved radial velocity field, showing a decreasing gradient in radial velocity along the optical bar from NE to SW, suggesting solid body rotation. This result agrees well with previous kinematical results (Valdez–Gutiérrez et al. 2000, and references therein). We believe that NGC 4449 presents solid body rotation (albeit at low rotation velocities) north of the optical center. Reliable fits are not possible in the southern sector of the disk, due to the chaotic motions at those locales. The inner H I kinematics (inner $13\overset{\prime}{.}4$) also shows a good correspondence with the optical radial velocities we find in this study.

In general, our kinematical and dynamical findings for the ionised gas in NGC 4449 are fully consistent within the framework of a past interaction with DDO 125.

MVG acknowledges support from a CONACyT scholarship number 114735. This work was partially supported by grants IN122298 of DGAPA–UNAM, 27984–E and 28507–E of CONACYT. The authors wish to thank Drs. D. Mayya, A. Luna and E. Brinks, for their comments and criticism pertinent to our study. Fruitful discussions with Drs. M. Bureau, I. Shlosman and V. Avila–Reese, enriched the last phase of this work and took place at the International Workshop in Astrophysics “Guillermo Haro 2001”. The authors are indebted to Prof. David Block for kindly assisting us with the grammatical content of our paper, and for discussions which greatly improved the scientific presentation of the contents. MVG thanks P. Scowen for providing her with his PhD Thesis, which was useful when performing comparisons with the present work. IP thanks J. Boulesteix and H. Plana for providing advice on the Adhoc package. We also thanks the anonymous referee for her/his insight and suggestions. This research has made use of the NASA/IPAC Extragalactic Database (NED) which is operated by the Jet Propulsion Laboratory, California Institute of Technology, under contract with the National Aeronautics and Space Administration.

REFERENCES

Arsenault, R., Roy, J.–R. 1988, A&A, 201, 199

Bajaja, E., Huchtmeier, W. K., Klein, U. 1994, A&A, 285, 385

Balick, B., Heckman, T. 1978, ApJ, 226, L7

Barnes, J. V., Hayes, D. S. 1982, IRS standard star manual, Kitt Peak National Observatory.

Block, D. L., Puerari, I., Takamiya, M., Abraham, R., Stockton, A., Robson, I., Holland, W. 2001, A&A, 371, 393

Böker, T., van der Marel, R. P., Mazzuca, L. et al. 2001, AJ, 121, 1473

Bomans, D. J., Chu, Y.-H., Hopp, U. 1997, AJ, 113, 1678

Borissova J., Georgiev L., Kurtev R. et al. 2000, Rev. Mex. Astron. Astrof., 36, 151

Boulesteix, J. 1993, ADHOC Reference manual, Marseille: Publications de l'Observatoire de Marseille

Burstein, D., Heiles, C. 1978, ApJ, 225, 40

Chyży, K. T., Beck, R., Kohle, S. et al. 2000, A&A, 355, 128

Crillon, R., Monnet, G. 1969, A&A, 1, 449

Della Ceca, R., Griffiths, R. E., Heckman, T. M. 1997, ApJ, 485, 581

de Vaucouleurs, G., de Vaucouleurs, A., Corwin, H. G. 1976, 2nd Ref. Cat. of Bright Galaxies. Austin: Univ. Texas Press. (RC2)

de Vaucouleurs, G., de Vaucouleurs, A., Corwin, H. G. 1991, 3rd Ref. Cat. of Bright Galaxies. New York: Springer–Verlag. (RC3)

Ferguson, A. M. N., Wyse, R. F. G, Gallagher, J. S. et al. 1996, AJ, 111, 2265

Firmani, C., D'Onghia, E., Avila–Reese, V. et al. 2000, MNRAS, 315, L29

Firmani, C., D'Onghia, E., Chincarini, G. et al. 2001, MNRAS, 321, 713

Fouque, P., Durand, N., Botinelli, L. et al. 1992, Catalogue of Optical Radial Velocities

Fuentes-Masip, O., Castañeda, H. O., Muñoz-Tuñón, C. 2000, AJ, 119, 2166

Gallagher, J. S., Hunter, D. A. 1984, ARA&A, 22, 37

Gelatt, A. E., Hunter, D. A., Gallagher, J. S. 2001, PASP, 113, 142

Hartmann, L. W., Geller, M. J., Huchra, J. P. 1986, AJ, 92, 1278

Hill, R. S., Fanelli, M. N., Smith, D. A. et al. 1998, ApJ, 507, 179

Hippelein, H. H. 1986, A&A, 160, 374

Hodge, P. W. 1969, ApJS, 18, 73

Hodge, P. W. 1983, AJ, 88, 1323

Hodge, P. W., Kennicutt, R. C. 1983, AJ, 88, 296

Hodge, P. W., Lee, M. G., Kennicutt, R. C. 1989, PASP, 101, 32

Hunter, D. A. 1982, ApJ, 260, 81

Hunter, D. A. 1997, PASP, 109, 937

Hunter, D. A., Gallagher, J. S. 1990, ApJ, 362, 480

Hunter, D. A., Gallagher, J. S. 1992, ApJ, 391, L9

Hunter, D. A., Gallagher, J. S. 1997, ApJ, 475, 65

Hunter, D. A., Wilcots, E. M., van Woerden, H. et al. 1998, ApJ, 495, L47

Hunter, D. A., van Woerden, H., Gallagher, J. S. 1999, AJ, 118, 2184

Hunter, D. A., Hunsberger, S. D., Roye, E. W. 2000a, ApJ, 542, 137

Hunter, D. A., Walker, C. E., Wilcots, E. M. 2000b, AJ, 119, 668

Kennicutt, R. C. 1984, ApJ, 287, 116

Kennicut, R. C., Hodge, P. 1986, ApJ, 306, 130

Kennicutt, R. C., Edgar, B. K., Hodge, P. W. 1989, ApJ, 337, 761

Kim, S.,Staveley–Smith, L., Dopita, M. A. et al. 1998, ApJ, 503, 674

Kingsburgh, R. L., McCall, M. L. 1998, AJ, 116, 2246

Kohle, S. 1999, PhD. thesis, Bonn University

Laval, A., Rosado, M., Boulesteix, J. 1992, A&A, 253, 213

Le Coarer, E., Rosado, M., Georgelin, Y. et al. 1993, A&A, 280, 365

Malumuth, E., Williams, T. B., Schommer, R.A. 1986, AJ, 91, 1295

Martin, C. L. 1998, ApJ, 506, 222

Mihalas, D., Binney, J. 1981, Galactic Astronomy, W.H. Freeman and Company (San Francisco), 503.

Otmianowska–Mazur, K. Chyży, K.T., Soida, M. et al. 2000, A&A, 359, 29

Parker, J. W., Garmany, C. D., Massey, P. et al. 1992, AJ, 103, 1205

Pleuss, P. O., Heller, C. H., Fricke, K. J. 2000, A&A, 361, 913

Reynolds, R. J. 1991, in IAU Symposium 144, The Disk–Halo Connection in Galaxies, Ed. H. Bloemen (Kluwer, Dordrecht), 67

Reynolds, R. J. 1993, in Back to the Galaxy, AIP Conf. Proc. 278, Eds. S. S. Holt & F. Verter (AIP, New York), 156

Rosado, M., Langarica, R., Bernal, A. et al. 1995, Rev. Mex. Astron. Astrof. Conf. Ser. 3, 268

Rosado, M., Laval, A., Le Coarer, E. et al. 1996, A&A, 308, 588

Rosado, M., Valdez–Gutiérrez, M., Georgiev, L., Arias, L., Borissova, J., Kurtev, R. 2001, AJ, 122, 194

Sabbadin, F., Bianchini, A. 1979, PASP, 91, 280

Sabbadin, F., Ortolani, S., Bianchini, A. 1984, A&A, 131, 1

Satyapal, S., Watson, D. M., Pipher, J. L. et al. 1997, ApJ, 483, 148

Schmidt, K.–H., Boller, T. 1992, Astron. Nachr. 313, 189

Scowen, P. A. 1992, PhD Thesis, Rice University

Seaquist, E. R., Bignell, R. C. 1978, ApJ, 226, L5

Shostak, G. S., Skillman, E. D. 1989, A&A, 214, 33

Spitzer, L. Jr. 1978, in Physical Processes in the Interstellar Medium, J. Willey & Sons, New York.

Strobel, N. V., Hodge, P. W., Kennicutt, R. C. 1991, ApJ, 383, 148

Theis, C. 1999, Rev. Mod. Astron., 12

Theis, C., Kohle, S. 2001, A&A, 370, 365

Tully, R. B. 1988, Nearby Galaxies Catalog, Cambridge University Press, Cambridge

Valdez–Gutiérrez, M., Rosado, M., Georgiev, L. et al. 2000, ASP Conference Series, 195, 346

Valdez–Gutiérrez, M., Rosado, M., Georgiev, L. et al. 2001, A&A, 366, 35

van den Bergh, S. 1981, AJ, 86, 1464

van Woerden, H., Bosma, A., Mebold, V. 1975, in "La Dynamique des Galaxies Spirales", Ed. L. Weliachew (Editions du Centre National de la Recherche Scientifique, Paris), 48

Vogler, A., Pietsch, W. 1997, A&A, 319, 459

Yoshida, M., Shimizu, Y., Koyano, H. et al. 1995, ASP Conference Series, 71, 207

Youngblood, A., Hunter, D. 1999, ApJ, 519, 55

This 2-column preprint was prepared with the AAS LaTeX macros v5.0.

TABLE 1

NGC 4449 GLOBAL PROPERTIES AND OBSERVED QUANTITIES

Parameter	Value	Reference
Name	NGC 4449	
Type[a]	I(B)m	Tully (1988)
R.A. (2000)[b]	$12^{\rm h}\ 28^{\rm m}\ 13\overset{\rm s}{.}1$	de Vaucouleurs et al. (1976)
Dec (2000)[b]	$+44^\circ\ 05'\ 43''$	
Distance[c]	3.7 Mpc	Bajaja et al. (1994)
B magnitude[d]	–18.5	Schmidt & Boller (1992)
Angular size[e]	$5\overset{\prime}{.}8\times4\overset{\prime}{.}5$	LEDA
Radial velocity[f]	211 km s^{-1}	NED
Axial ratio	0.77	Tully (1988)
Inclination	43°	Tully (1988)
P.A.[g]	45°	de Vaucouleurs et al. (1991)
M_{tot}[c]	7×10^{10} $M_\odot$	Bajaja et al. (1994)
$M_{\rm HI}$[c]	2.3×10^{9} $M_\odot$	Bajaja et al. (1994)
HI extent[c]	43×70 kpc	Bajaja et al. (1994)
L_B[h]	2.1×10^{9} ${L^B}_\odot$	Martin (1998)
$(M/L)_*$[h]	11	Martin (1998)
SFR[i]	0.47 $M_\odot$ yr^{-1}	Hunter et al. (1999)
Log L(Hα)[i]	40.82 erg s^{-1}	Hunter et al. (1999)

[a] Morphologycal type.

[b] Photometric center position.

[c] Distance, total mass, H I mass and H I extent adopted in this work.

[d] Absolute B magnitude.

[e] Optical extent. Isophotal diameter at 25^m per arcsecond squared.

[f] Optical heliocentric radial velocity. The error in this measurement is ± 15 km s^{-1}.

[g] Position angle measured on the stellar component.

[h] B-band luminosity (where ${M^B}_\odot$=5.48) and stellar mass to blue light ratio in absence of dark matter.

[i] Star formation rate and log of the Hα luminosity.

TABLE 2
PUMA OBSERVATIONS OF NGC 4449

Mode[a]	Filter	bin[b]	t[c]	Date	Comments
FP	Hα	2	5760	09.01.1997	2 datacubes
FP	[SII]	2	5760	20.06.1998	2 datacubes
D	Hα	2	120	10.01.1997	
D	[SII]	2	120	10.01.1997	
D	[OIII]	2	300	10.01.1997	
D	[NII]	2	120	10.01.1997	
D	Hα	1	60	20.06.1998	
D	[SII]	1	120	20.06.1998	
D	[OIII]	1	120	20.06.1998	
D	[NII]	1	120	20.06.1998	
D	Hα	1	30	20.06.1998	Standard star
D	Hα	1	30	20.06.1998	Standard star
D	Hα	4	60	11.02.1999	Position 1
D	Hα	4	300	11.02.1999	
D	Hα	4	60	11.02.1999	Position 2
D	Hα	4	300	11.02.1999	
D	Hα	4	60	11.02.1999	Position 3
D	Hα	4	300	11.02.1999	

[a] Mode of observation: FP= scanning Fabry–Perot observations, D= direct imaging.

[b] Binning.

[c] Total integration time in seconds.

Table 3
Photometry for the H II regions in NGC 4449

ID	Other IDs	D (pc)	log F(Hα) erg cm^{-2} s^{-1}	log L(Hα) erg s^{-1}	log S(Hα) erg cm^{-2} s^{-1} steradian^{-1}
M1	3	59.1	-13.91	37.31	-4.22
M2	4	68.1	-13.67	37.54	-4.11
M3	6,7, V1	129.9	-12.78	38.44	-3.78
M4	8, V2	49.0	-13.91	37.30	-4.07
M5	9, V3	67.7	-13.58	37.63	-4.01
M6	12, V4	52.1	-13.94	37.28	-4.14
M7	13,14,16, V5	99.4	-12.96	38.25	-3.73
M8	15, V6	66.4	-13.78	37.42	-4.20
M9	17	48.4	-13.61	37.60	-3.75
M10	18,19, V7	39.1	-14.33	36.89	-4.28
M11	20, V8	67.9	-13.09	38.12	-3.53
M12	21, V9	57.1	-13.60	37.62	-3.88
M13	22, V10	51.1	-14.03	37.18	-4.22
M14	23, V8	76.1	-12.95	38.26	-3.49
M15	24, V8	103.0	-12.61	38.60	-3.41
M16	26,27, V11	80.7	-13.43	37.78	-4.02
M17	28,31, V12	68.2	-13.46	37.75	-3.90
M18	34,35,37,38,39,41,43, V15	183.3	-12.21	39.00	-3.51
M19	36	45.3	-13.85	37.36	-3.94
M20	40, V16	49.4	-13.78	37.44	-3.94
M21	44, V17	105.6	-13.47	37.74	-4.29
M22	45	34.7	-14.17	37.05	-4.02
M23	47, V18	94.1	-12.91	38.31	-3.63
M24	48,54, V19,V23	89.7	-13.38	37.84	-4.06
M25	50,55,59, V20	164.5	-12.13	39.09	-3.33
M26	51,58, V21	87.6	-13.27	37.94	-3.93
M27	52,56,57, V24	83.2	-13.12	38.09	-3.73
M28	53, V22	91.0	-13.80	37.41	-4.49
M29	62,64	83.2	-13.59	37.63	-4.20
M30	63	71.8	-13.65	37.56	-4.14
M31	73	63.6	-13.99	37.23	-4.37
M32	75, V27	184.4	-11.68	39.53	-2.98
M33	76, V28	63.5	-13.33	37.88	-3.71
M34	78	82.0	-13.44	37.78	-4.04
M35	79, V29	83.3	-13.21	38.00	-3.83
M36	81,82, V30	127.5	-12.66	38.55	-3.65
M37	83	71.2	-13.67	37.55	-4.14
M38	84, V31	66.6	-13.50	37.72	-3.92
M39	86, V32	57.8	-13.66	37.56	-3.95
M40	89, V33	104.5	-12.81	38.40	-3.61
M41	90, V32	38.8	-14.17	37.04	-4.12
M42	91	60.3	-13.07	38.15	-3.40
M43	92,103	75.5	-13.24	37.98	-3.77
M44	93,107,108, V34	138.3	-12.84	38.38	-3.89
M45	94,99,116	134.4	-12.60	38.61	-3.63
M46	96, V35	82.2	-13.72	37.50	-4.32
M47	98, 105, V36	77.6	-13.58	37.63	-4.13
M48	100, V37	90.1	-13.63	37.59	-4.31
M49	108, V38	130.4	-12.35	38.86	-3.35
M50	111, V39	64.4	-13.35	37.87	-3.74
M51	112, V40	117.9	-12.56	38.66	-3.47
M52	113,115, V41	71.6	-13.43	37.78	-3.92
M53	114, V42	115.7	-12.72	38.50	-3.62

Table 3—*Continued*

ID	Other IDs	D (pc)	log F(Hα) erg cm^{-2} s^{-1}	log L(Hα) erg s^{-1}	log S(Hα) erg cm^{-2} s^{-1} steradian^{-1}
M54	117,121, V39	109.5	-12.73	38.48	-3.58
M55	118, V43	66.0	-13.87	37.34	-4.28
M56	119,123, V44	87.2	-12.78	38.44	-3.43
M57	125, V45	94.5	-12.84	38.38	-3.56
M58	126,127, V46	151.4	-12.30	38.91	-3.43
M59	128,129, V41	91.0	-12.94	38.27	-3.64
M60	131,137, V41	67.1	-13.22	38.00	-3.64
M61	132,134, V45	97.8	-12.62	38.59	-3.37
M62	133, V47	112.9	-12.53	38.67	-3.41
M63	138,146,158, V49	123.8	-12.48	38.73	-3.44
M64	139,140, V48	72.4	-13.30	37.92	-3.79
M65	142,150,151,157, V50	136.0	-12.33	38.89	-3.37
M66	152, V51	92.5	-13.03	38.19	-3.73
M67	153,159, V49	86.4	-12.90	38.31	-3.54
M68	161, V52	85.0	-13.08	38.13	-3.71
M69	165,169,172,186,188, V53	128.6	-12.66	38.56	-3.65
M70	167	54.8	-13.60	37.61	-3.85
M71	168, V55	64.8	-13.40	37.81	-3.80
M72	170,171, V56	70.9	-12.87	38.34	-3.34
M73	173	51.4	-13.79	37.43	-3.98
M74	180, V58	77.9	-13.31	37.90	-3.87
M75	181,182, V59	98.5	-13.17	38.05	-3.93
M76	183, V60	87.5	-13.20	38.00	-3.86
M77	185,187, V61	142.6	-12.43	38.79	-3.51
M78	191	70.6	-13.07	38.15	-3.54
M79	192	100.7	-12.64	38.58	-3.41
M80	199,200	51.1	-13.58	37.63	-3.77
M81	202	93.9	-13.21	38.01	-3.93
M82	203, V65	84.7	-12.85	38.35	-3.48
M83	204, V66	81.7	-13.60	37.61	-4.20
M84	208,209, V67	89.5	-12.70	38.50	-3.38
M85	212, V69	107.4	-12.66	38.55	-3.49
M86	218,219, V71	111.4	-12.98	38.24	-3.84
M87	220, V72	95.9	-12.29	38.91	-3.03
M88	221,222, V73	78.7	-12.50	38.70	-3.07
M89	224,225,227, V74	132.0	-12.85	38.37	-3.86
M90	226,234, V73	78.2	-12.51	38.70	-3.07
M91	230,231, V75	108.0	-12.86	38.36	-3.70
M92	233,235, V76	56.1	-13.93	37.28	-4.20
M93	237,238, V77	98.4	-13.24	37.98	-3.99
M94	239,240,244, V78, V79	149.9	-12.99	38.22	-4.12
M95	245,247,248, V80	151.2	-12.87	38.35	-4.00
M96	249, V81	67.8	-13.71	37.50	-4.15
M97	250,252, V82	127.6	-13.25	37.96	-4.23
M98	251, V82	81.7	-13.63	37.58	-4.23
M99	nucleus, V84	163.0	-11.89	39.32	-3.07
M100	h61	67.0	-12.84	38.37	-3.26
M101	h66	69.5	-12.45	38.75	-2.91

TABLE 4
MEASURED KINEMATICAL PARAMETERS FOR THE H II REGIONS IN NGC 4449

ID	Other IDs	v_1 (km s^{-1})	v_2 (km s^{-1})	σ_1 (km s^{-1})	σ_2 (km s^{-1})	Stars	comments
V1	6	218	···	17.6	···	1N, 28	a
V2	8u	230	···	21.2	···	1N, ···	a, dig contaminated?
V3	9	220	···	18.5	···	···	s
V4	12	227	···	17.6	···	···	a
V5	13,14,16	231	···	22.1	···	2N, 23	a
V6	15	228	···	22.9	···	···	a
V7	18u,19u	220	···	4.3	···	3O, ···	a
V8	20,23,24	236	···	24.7	···	2N, 24	a
V9	21u	243	···	27.3	···	2N, ···	a, wide wings, dig?
V10	22	211	···	17.6	···	3O, ···	a
V11	26,27	201	···	19.5	···	3O, 35	a
V12	28,31	244	···	26.4	···	··· , 8	s
V13	29	254	···	11.8	···	···	a
V14	33u,36	231	···	23.9	···	···	s
V15	34,35,37,38,39,41,43	244	···	23.9	···	4N, 13	s
V16	40	231	···	26.4	···	···	s
V17	44	197	···	14.8	···	···	a
V18	47	211	···	22.1	···	···	a, red broad wing
V19	48	246	···	15.1	···	···	a
V20	50,55,59	235	···	21.2	···	5N, 2	a
V21	51,58,63u	207	···	19.5	···	··· , 44	a
V22	53	183	···	17.6	···	···	a
V23	54	243	···	22.1	···	···	a
V24	56,57	228	···	20.4	···	··· , 15	a
V25	72	232	···	27.3	···	···	a, broad red wing
V26	74,80	230	···	22.1	···	···	s
V27	75,91	231	···	22.1	···	6N, 1	a
V28	76	236	···	22.1	···	9N, ···	a
V29	79	246	···	28.2	···	6N, ···	a
V30	81,82	211	···	17.6	···	10B, 20	a
V31	84,85,97	216	···	33.2	···	···	a
V32	86,90u	220	···	17.6	···	···	s
V33	89	207	···	19.5	···	11B, 33	a
V34	93,107,108	216	352	26.2	12.9	···	double
V35	96	205	···	14.5	···	···	a
V36	98, 105	196	···	20.4	···	8B, ···	a
V37	100	192	···	17.6	···	···	a
V38	108	218	···	19.5	···	11B, 34	a
V39	111,117,121	226	···	29.0	···	10B, 30	s
V40	112	242	···	24.7	···	9N, 6	a
V41	113,115,128,129,131,137	223	···	20.4	···	12B, 39	a, wide wings
V42	114	221	···	17.6	···	12B, 38	a
V43	118	205	···	20.4	···	···	a
V44	119,123	205	···	18.5	···	8B, 50	a
V45	125u,132	216	···	18.5	···	8B, 49	a
V46	126,127	236	···	26.4	···	13N, 4	s
V47	133	207	···	22.1	···	11B, 32	a
V48	139,140	219	···	26.4	···	···	s, broad red wing
V49	146,147,153,158,159	222	···	29.0	···	14B, 31	a
V50	151	219	···	30.7	···	14B, ···	a
V51	152	219	···	22.1	···	···	a, wide wings
V52	161	237	···	35.7	···	12B, ···	s, wide wings
V53	165,169,172	203	···	23.4	···	15N, 22	a

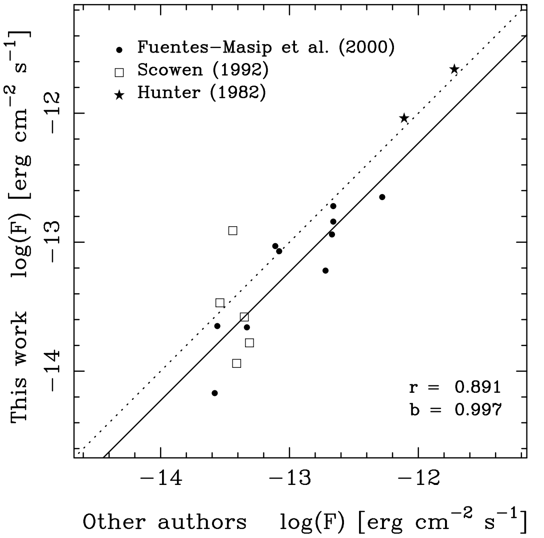

Fig. 3.— A comparison between our flux determinations with published fluxes as determined in other investigations. The solid line is our best fit to Fuentes-Masip et al. (2000), while the dotted one represents the diagonal. Values of the correlation coefficient (r) and the slope (b) of the least squares fit are given at bottom right.

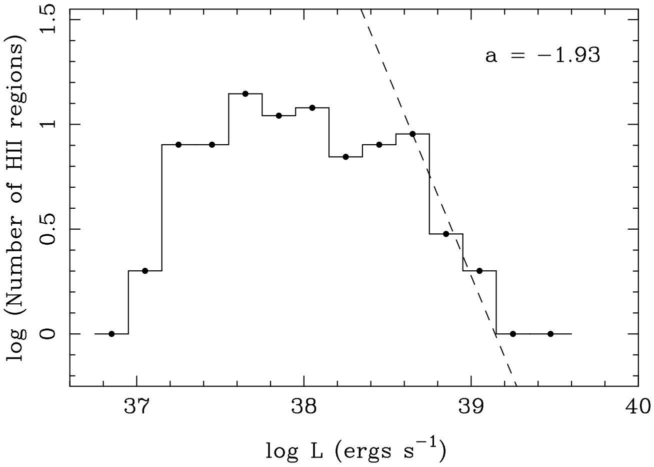

Fig. 5.— The Hα luminosity function for the H II regions in NGC 4449. The dashed line is the least squares fit to a power law. The value of the slope is given at top right.

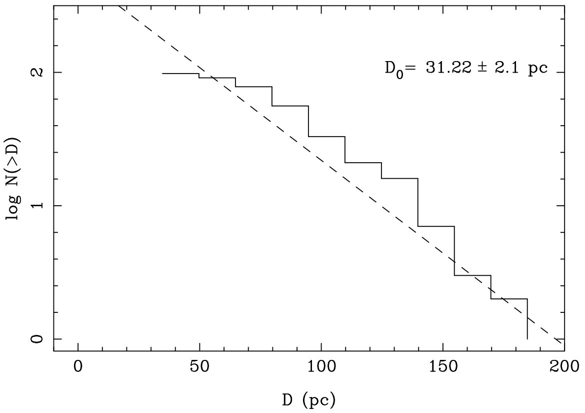

Fig. 6.— The cumulative size distribution for the H II regions in NGC 4449, where the dashed straight line represents a least squares fit. The value for the characteristic diameter is given in the top right hand corner.

Table 4—*Continued*

ID	Other IDs	v_1 (km s^{-1})	v_2 (km s^{-1})	σ_1 (km s^{-1})	σ_2 (km s^{-1})	Stars	comments
V54	166	227	···	32.4	···	··· , 18	a, dig contaminated?
V55	168	223	···	37.4	···	··· , 11	a
V56	170	192	256	20.4	19.5	16B, 37	double
V57	178,190	219	···	29.0	···	16B, 37	a
V58	180	223	···	36.5	···	···	s, top flated
V59	181,182	215	···	22.1	···	··· , 51	a
V60	183	189	···	26.4	···	18B, ···	a, broad red wing
V61	185,187	220	···	26.4	···	17N, 9	a, double?, SNR
V62	186	205	···	30.7	···	···	a, broad red wing
V63	192	218	···	26.4	···	17N, 10	a, SNR
V64	197	188	253	20.4	20.4	18B, 45	double
V65	203	185	255.0	19.5	17.6	18B, 42	double
V66	204	207	···	20.4	···	···	a, broad blue wing
V67	208,209	197	···	26.4	···	18B, 40	a
V68	211	218	···	19.5	···	···	a
V69	212	205	···	23.8	···	18B, 46	a
V70	213,217	222	···	29.0	···	··· , 21	s
V71	218,219	220	···	20.4	···	19N, 14	a
V72	220,h66	189	···	26.4	···	18B, 41	a
V73	221,222,226	196	···	26.4	···	18B, 43	a
V74	224,225,227	215	···	22.1	···	19N, 7	s
V75	230,231	219	···	23.4	···	19N, 12	s
V76	233u,235u	199	288	26.4	22.1	···	double
V77	237,238	210	···	17.6	···	20O, 27	a
V78	239,240	211	···	17.6	···	22O, 56	a
V79	244	218	···	17.6	···	22O, 56	s
V80	245,247,248	214	···	15.8	···	22O, 57	a
V81	249	205	···	28.1	···	···	a
V82	250,251,252	192	···	21.2	···	···	a, broad red wing
V83	h61	216	···	28.1	···	16B, 37	a
V84	nucleus	220	···	30.7	···	16B, 37	a

Table 5
Aperture positions for search of Hα emission

Position	R. A. (B1950.0)	Dec (B1950.0)	Hunter ID
1	12 25 04	43 59 11	···
2	12 25 04	44 14 08	Z2
3	12 27 05	44 29 08	Z1

Note.—Units for right ascension are hours, minutes and seconds. Those for declination are degrees, arcminutes and arcseconds. The cross identifications in column 4, are based on the work of Hunter et al. (2000b).

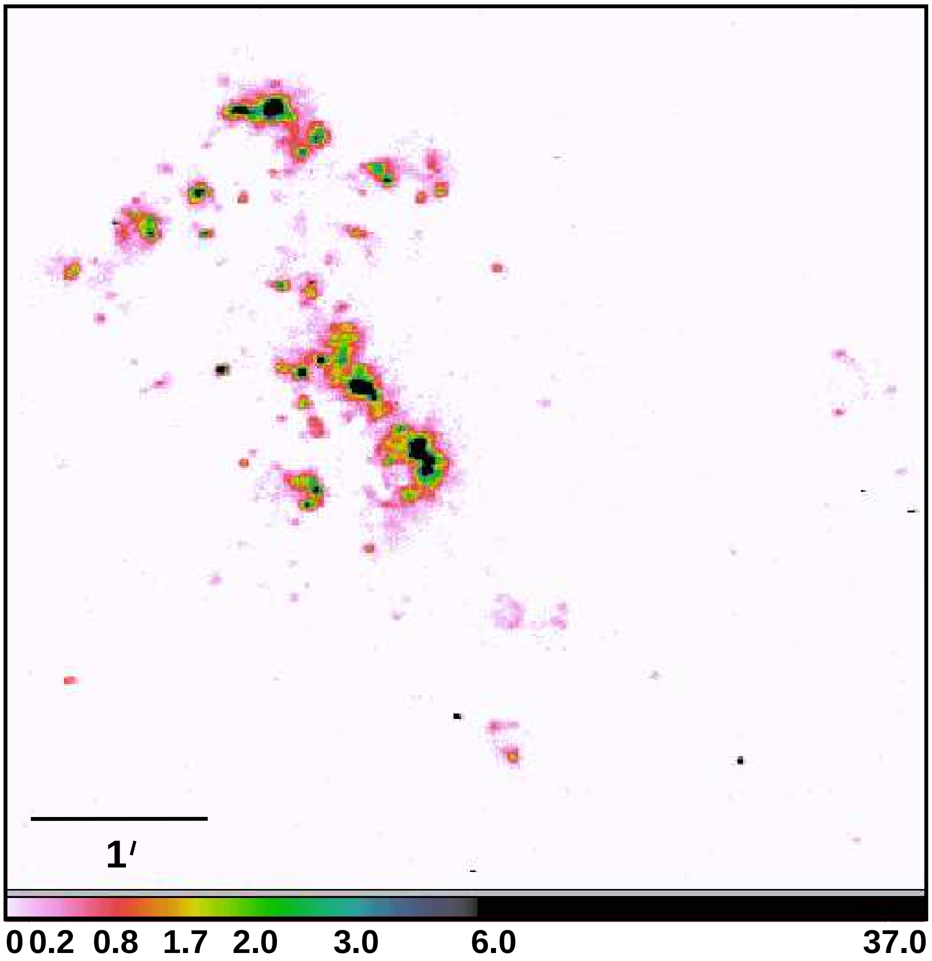

Fig. 1.— A flux–calibrated Hα image of NGC 4449, free of diffuse emission (see text for further details). The colors are related to counts sec^{-1}. In order to secure Hα fluxes, luminosities and surface brightnesses, multiplications by factors of 1.018×10^{-15} erg cm^{-2} s^{-1}, 1.66×10^{36} erg s^{-1} and 1.266×10^{-4} erg cm^{-2} s^{-1} steradian^{-1}, respectively, are necessitated. The scale is indicated at bottom left. North is up; East to the left.

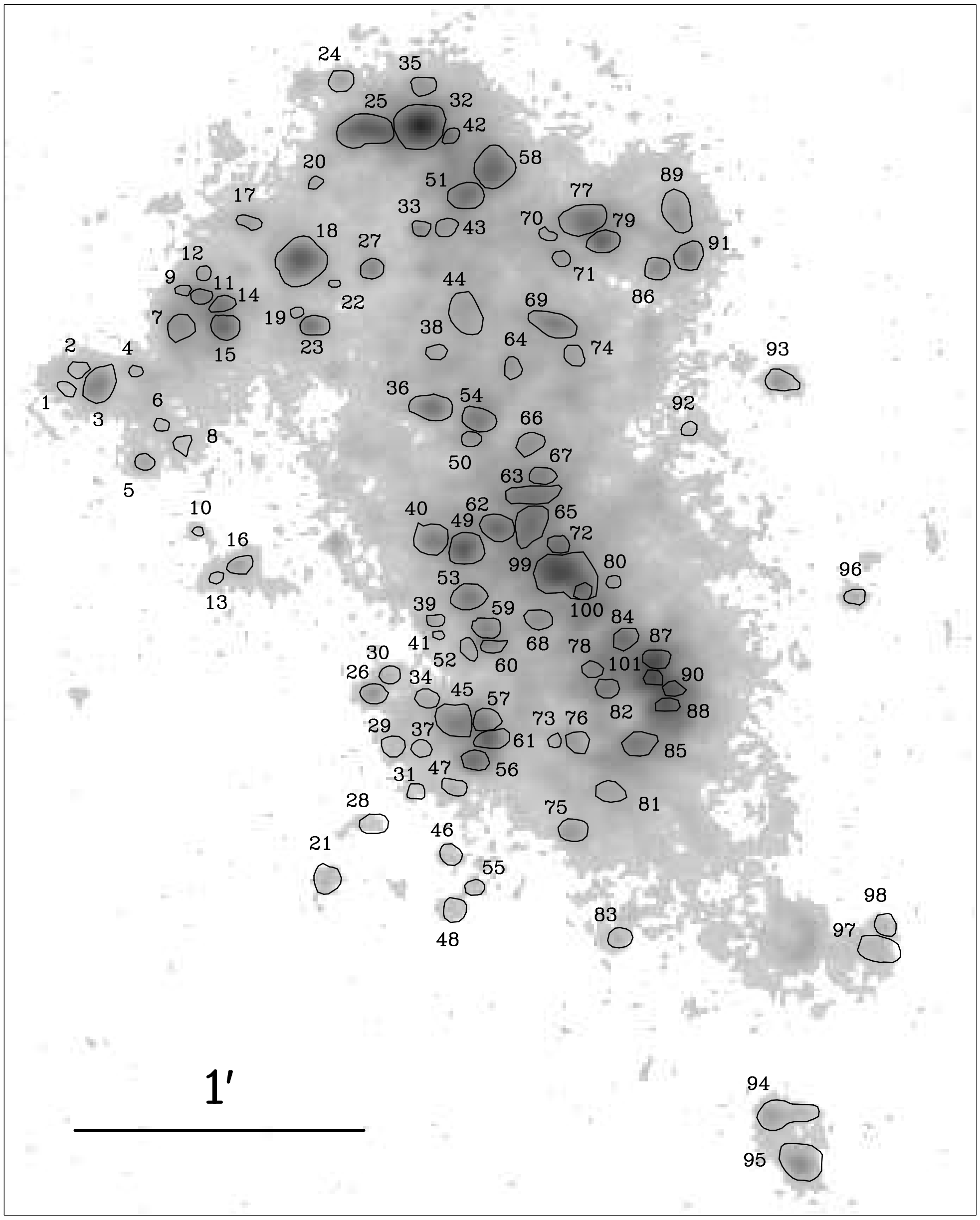

Fig. 2.— Polygonal apertures (defined without diffuse emission; see Figure 1) were used to obtain Hα fluxes from the H II region population in NGC 4449. In order to display weak features, we adopted a logarithmic scale for the gray levels. See text for further details. Numbers correspond to our "M" sources in Table 3. The scale is indicated at bottom left. North is up and East to the left.

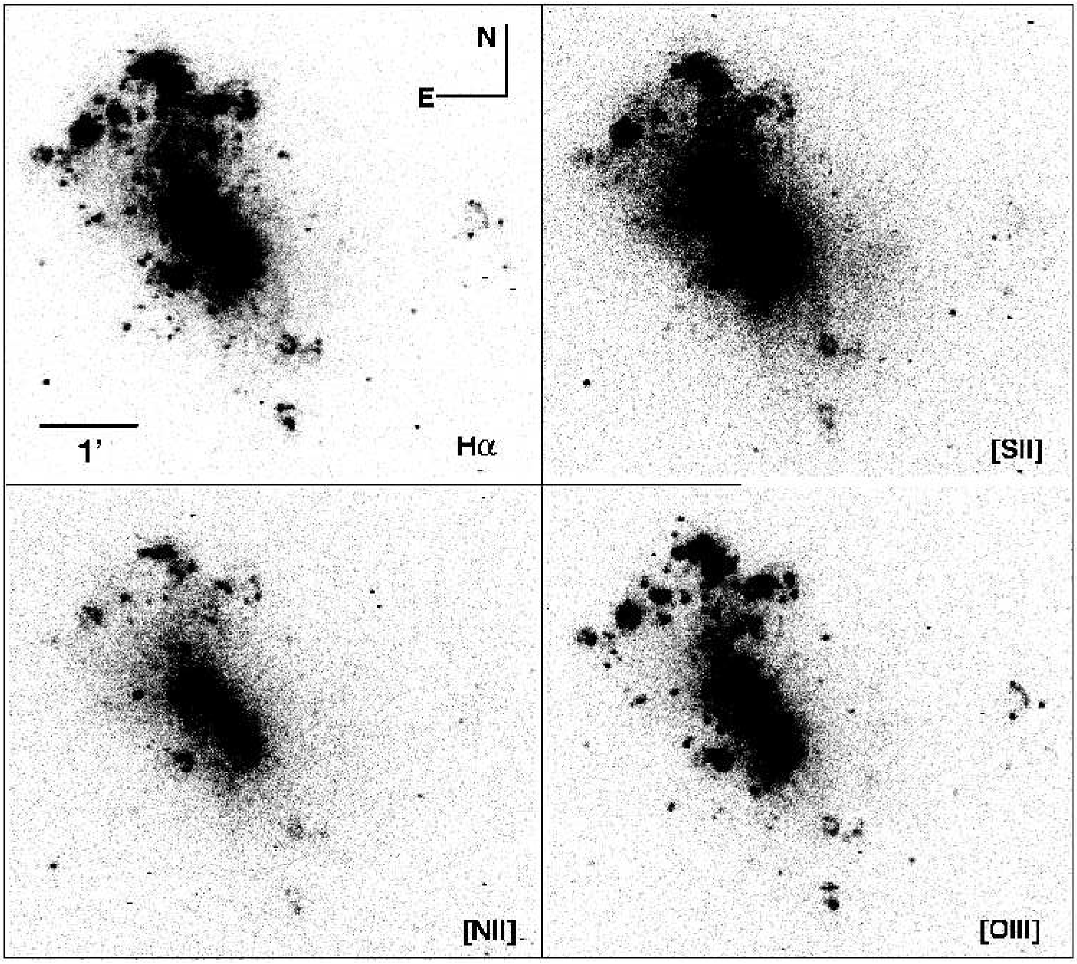

Fig. 4.— Direct images of NGC 4449 in the lines of Hα, [S II], [N II] and [O III]. The exposure times are those reported in Table 2. The scale and the orientation are indicated in the first panel.

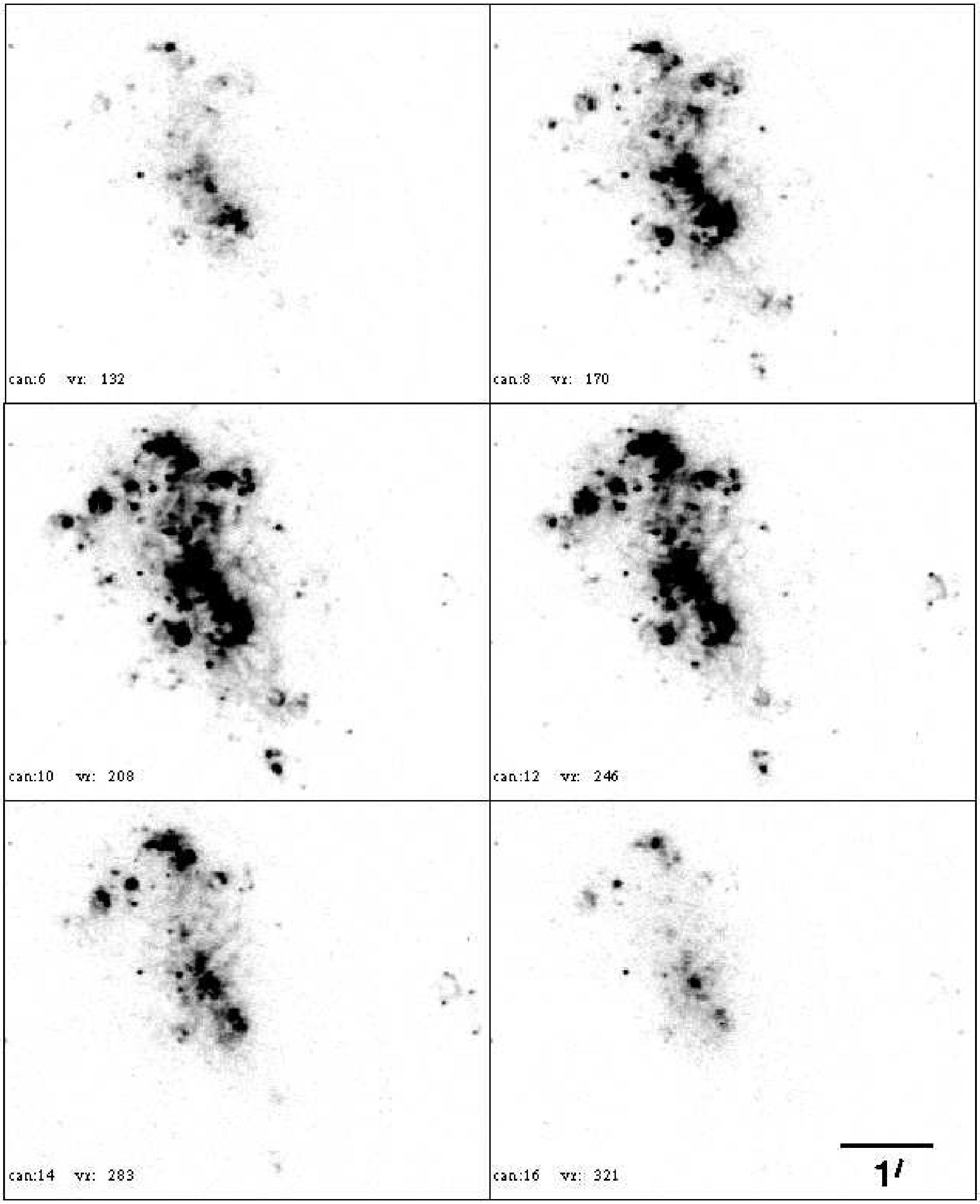

Fig. 7.— NGC 4449 Hα radial velocity maps. The channel number as well as the heliocentric radial velocity (in km s^{-1}) are indicated in each panel. The scale is indicated in the panel corresponding to channel 16, at bottom right.

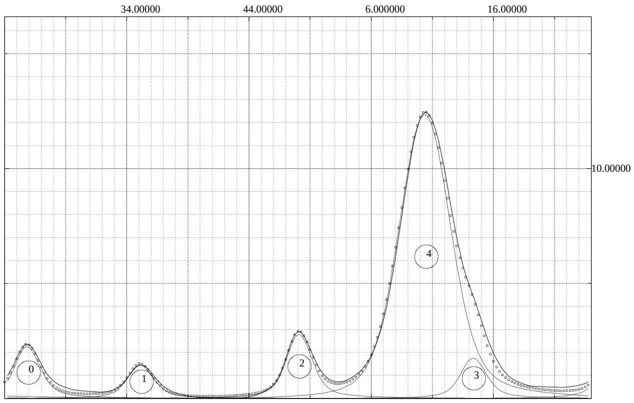

Fig. 8.— The observed Hα global radial velocity distribution in NGC 4449 (see text for details). The horizontal and vertical axes correspond to the channel number and intensity (arbitrary units), respectively. The fit to the sky–emission lines has been performed by means of curve numbers 0, 1, 2 and 3 (see text for details).

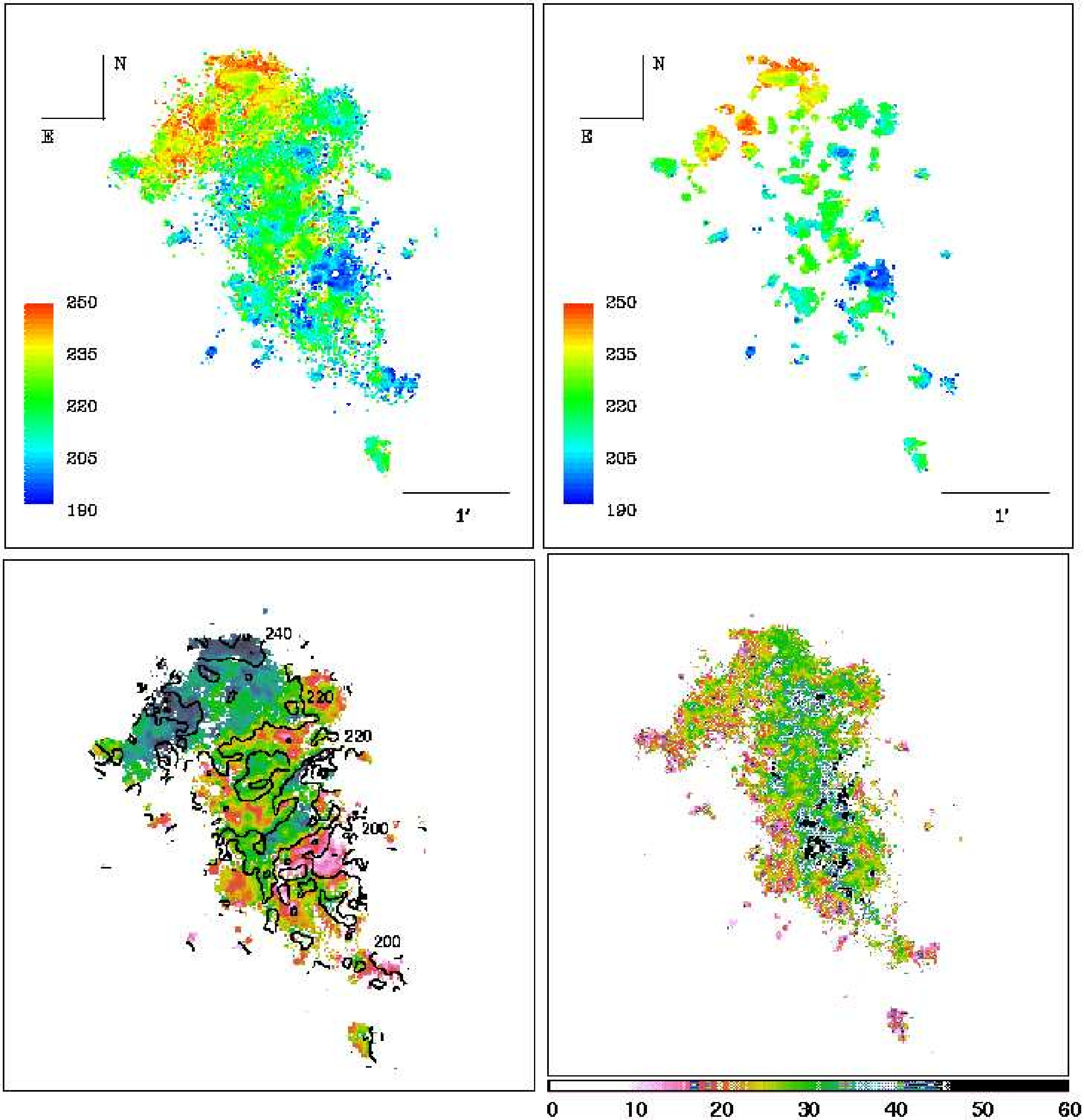

Fig. 9.— Top left: The observed heliocentric radial velocity field for the global content of ionized gas (including the diffuse emission component). Top right: As in the left panel, but for the ionized gas locally embedded in H II regions. Bottom left: Iso–velocities superimposed on the NGC 4449 radial velocity field. Bottom right: A superposition of the velocity dispersion field. Both bottom panels pertain to the global content of ionized gas in NGC 4449. In the radial velocity fields we have selected a palette which better enhances the gradient in velocity along the body of the galaxy (see text for details). The colors are related to heliocentric velocities. Velocity dispersions are given in km s^{-1}. The scale and the orientation are indicated.

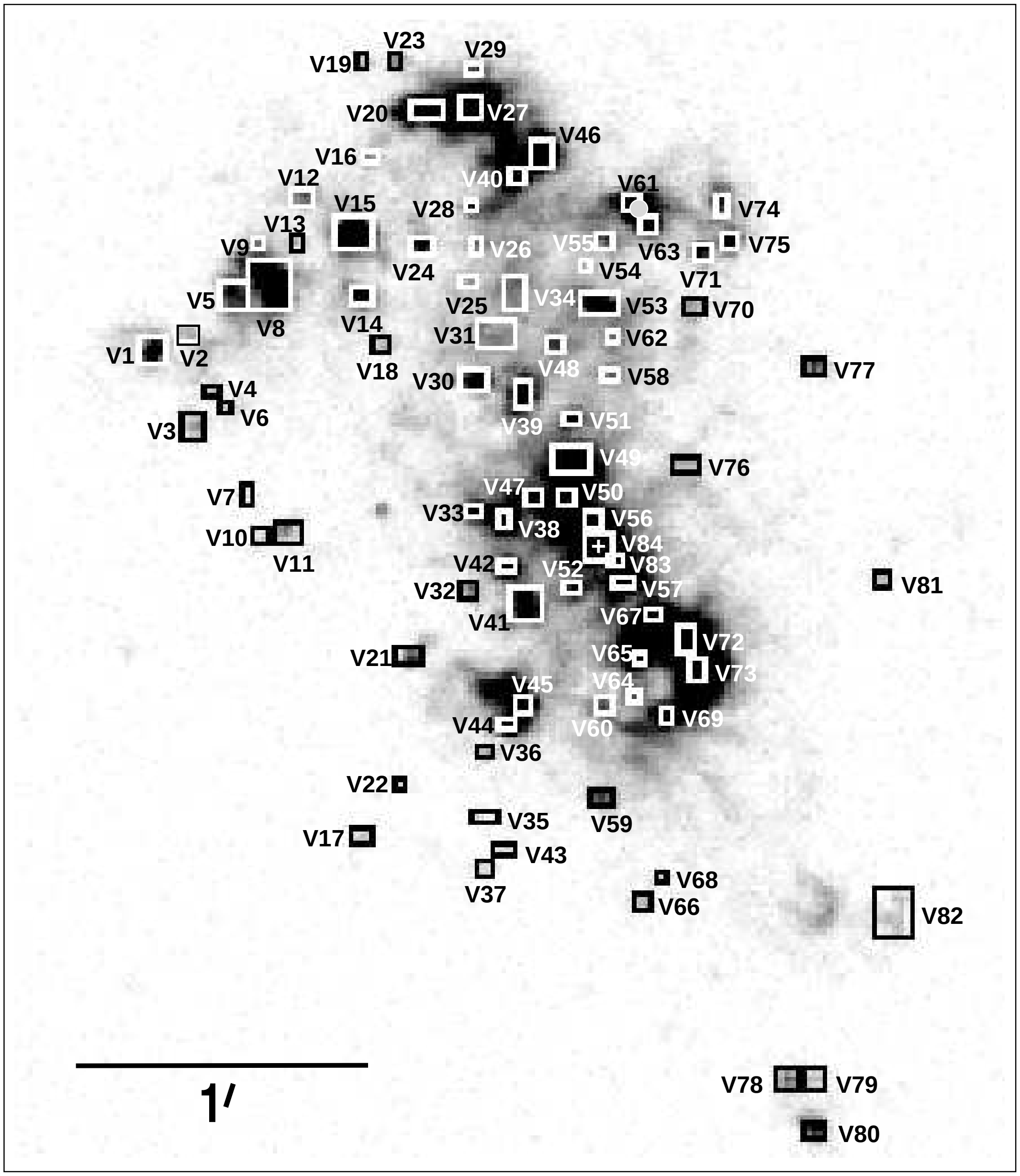

Fig. 10.— Our Hα monochromatic image of NGC 4449. The diffuse component as well as the H II region and filament populations, are readily noted. The boxes correspond to locales where we performed our kinematical analysis. The supernova remnant SB187 (embedded in our region V61) and the photometric center are indicated by a filled circle and by a cross, respectively. The scale is indicated at bottom left. North is up; East to the left.

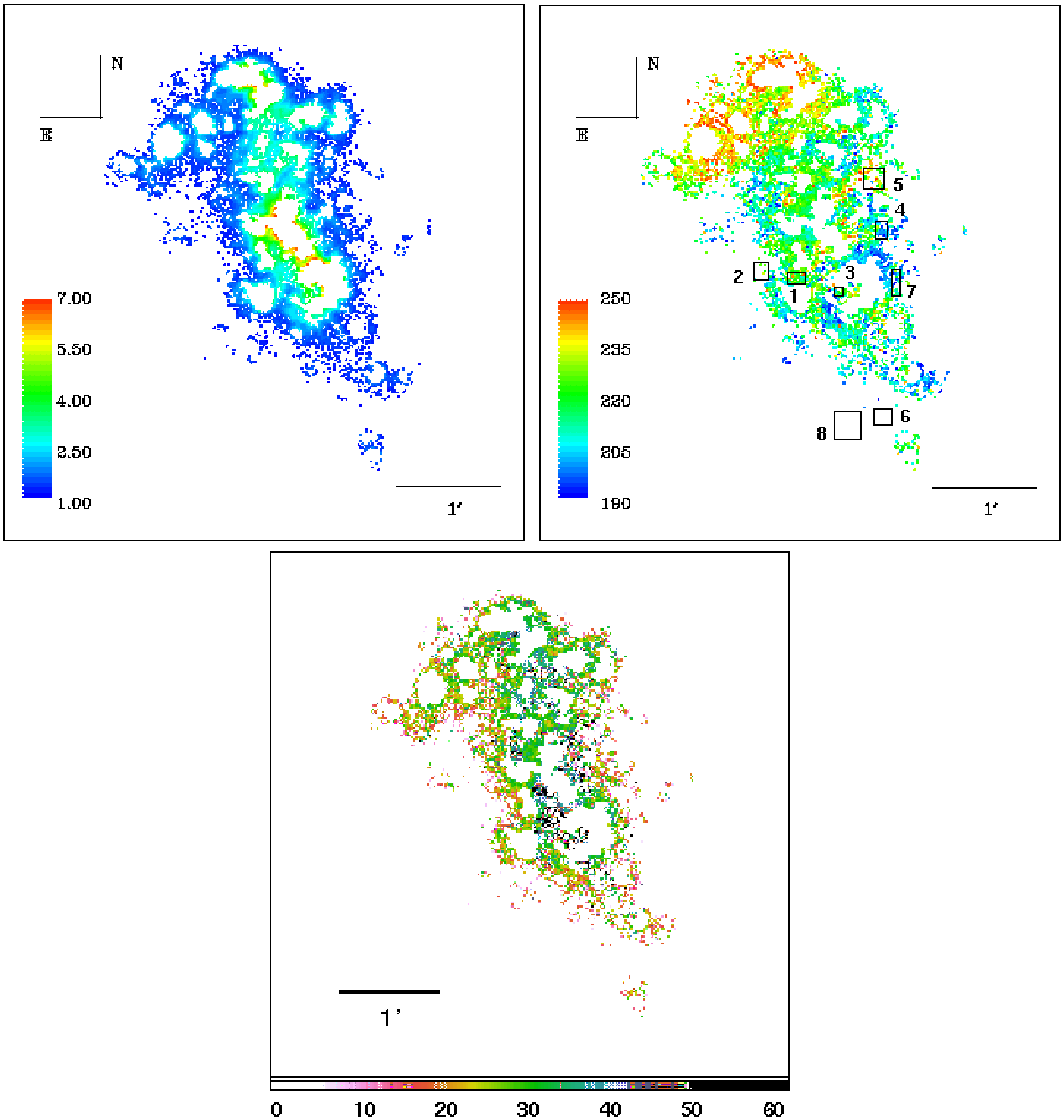

Fig. 11.— The widespread DIG component in NGC 4449. Top left: DIG intensities. Values are given in counts s^{-1}, and are indicated in the respective palette. In order to determine Hα fluxes, luminosities and surface brightnesses, multiplications by factors of 2.545×10^{-16} erg cm^{-2} s^{-1}, 4.17×10^{35} erg s^{-1} and 3.165×10^{-5} erg cm^{-2} s^{-1} steradian^{-1}, respectively, are required. Top right: The observed heliocentric radial velocity field. The boxes correspond to the locations of Malumuth et al. (1986); see text for further details. Bottom: The velocity dispersion field of NGC 4449. Values are given in km s^{-1} in the latter two maps. Spatial orientation and the scale are indicated.

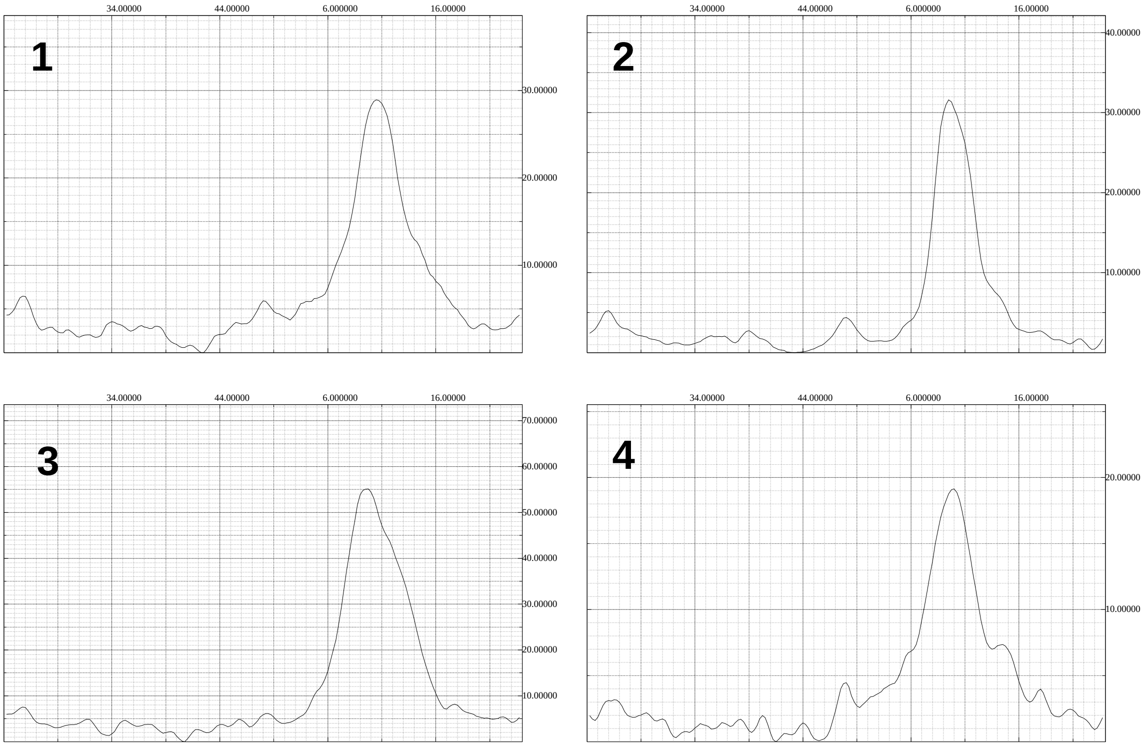

Fig. 12.— Typical DIG profiles found in NGC 4449. The numbers in the left hand corners correspond to the locales studied by Malumuth et al. (1986). Vertical and horizontal axes correspond to intensity (arbitrary units) and to channel number, respectively.

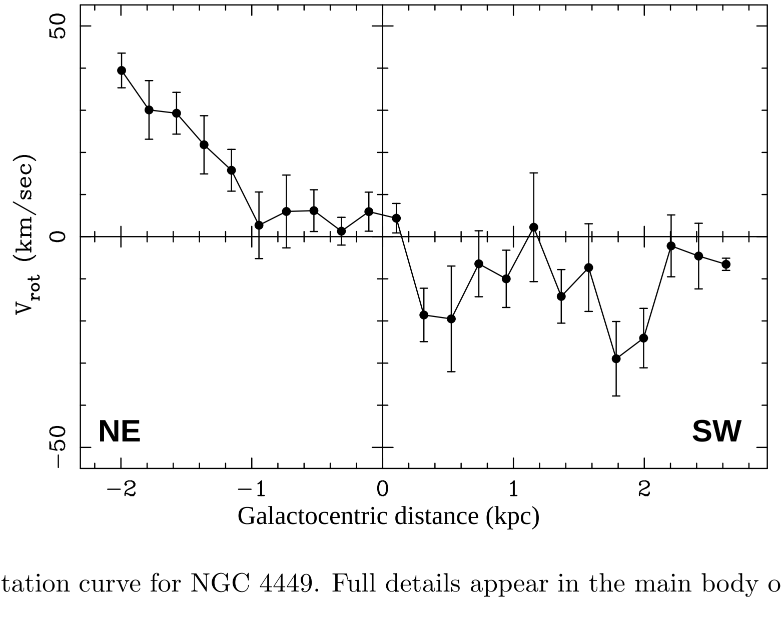

Fig. 13.— Our Hα rotation curve for NGC 4449. Full details appear in the main body of the paper.